

## RESEARCH ARTICLE



WILEY

# Morpho-physiological properties and connectivity of vasoactive intestinal polypeptide-expressing interneurons in the mouse hippocampal dentate gyrus

Yu-Ting Wei<sup>1</sup> | Jei-Wei Wu<sup>1</sup> | Chia-Wei Yeh<sup>1</sup> | Hung-Chang Shen<sup>1</sup> |  
Kun-Pin Wu<sup>2</sup> | Imre Vida<sup>3</sup> | Cheng-Chang Lien<sup>1,4</sup>

<sup>1</sup>Institute of Neuroscience, National Yang-Ming University, Taipei, Taiwan

<sup>2</sup>Institute of Biomedical Informatics, National Yang-Ming University, Taipei, Taiwan

<sup>3</sup>Institute for Integrative Neuroanatomy, Charité - Universitätsmedizin Berlin, Berlin, Germany

<sup>4</sup>Brain Research Center, National Yang-Ming University, Taipei, Taiwan

## Correspondence

Cheng-Chang Lien, Institute of Neuroscience, National Yang-Ming University, 155, Section 2, Li-Nong Street, Taipei 112, Taiwan.  
Email: cclien@ym.edu.tw

## Funding information

Deutsche Forschungsgemeinschaft, Grant/Award Number: 384230557; Ministry of Science and Technology, Grant/Award Number: 106-2923-B-010-001-MY3; National Health Research Institutes, Grant/Award Number: NHRI-EX109-10814NI

## Abstract

The hippocampus is a key brain structure for cognitive and emotional functions. Among the hippocampal subregions, the dentate gyrus (DG) is the first station that receives multimodal sensory information from the cortex. Local-circuit inhibitory GABAergic interneurons (INs) regulate the excitation–inhibition balance in the DG principal neurons (PNs) and therefore are critical for information processing. Similar to PNs, GABAergic INs also receive distinct inhibitory inputs. Among various classes of INs, vasoactive intestinal polypeptide-expressing (VIP<sup>+</sup>) INs preferentially target other INs in several brain regions and thereby directly modulate the GABAergic system. However, the morpho-physiological characteristics and postsynaptic targets of VIP<sup>+</sup> INs in the DG are poorly understood. Here, we report that VIP<sup>+</sup> INs in the mouse DG are highly heterogeneous based on their morpho-physiological characteristics. In approximately two-thirds of morphologically reconstructed cells, their axons ramify in the hilus. The remaining cells project their axons exclusively to the molecular layer (15%), to both the molecular layer and hilus (10%), or throughout the entire DG layers (8%). Generally, VIP<sup>+</sup> INs display variable intrinsic properties and discharge patterns without clear correlation with their morphologies. Finally, VIP<sup>+</sup> INs are recruited with a long latency in response to theta-band cortical inputs and preferentially innervate GABAergic INs over glutamatergic PNs. In summary, VIP<sup>+</sup> INs in the DG are composed of highly diverse subpopulations and control the DG output via disinhibition.

## KEYWORDS

connectivity, dentate gyrus, disinhibition, GABA, interneuron, morphology

## 1 | INTRODUCTION

The mammalian hippocampus is a key brain structure for episodic memory, spatial navigation, and stress-related emotional behaviors (Fanselow & Dong, 2010; Kheirbek et al., 2013; Milner, Corkin, & Teuber, 1968; Scoville & Milner, 1957). The dentate gyrus (DG), which receives multimodal sensory information from the cortex, is believed to support multiple mnemonic functions (Hainmueller & Bartos,

2020). Granule cells (GCs) constitute the vast majority of neuronal populations of the DG and integrate cortical inputs with low efficiency and generate sparse activity (Kress, Dowling, Meeks, & Mennerick, 2008; Krueppel, Remy, & Beck, 2011). Sparse GC activation provides a cellular mechanism to transform cortical information into distinct representations, which is crucial in contextual learning and pattern separation (Kheirbek et al., 2013; Leutgeb, Leutgeb, Moser, & Moser, 2007). Local-circuit GABAergic inhibitory interneurons

(INs) in the DG provide spatiotemporal dynamic inhibition in GCs in response to cortical input and are thereby contributed critically to the control of input–output transformations in GCs (Armstrong, Szabadics, Tamás, & Soltesz, 2011; Chiang et al., 2012; Ewell & Jones, 2010; Hefft & Jonas, 2005; Hsu, Lee, Tai, & Lien, 2016; Lee et al., 2016; Liu, Cheng, & Lien, 2014).

Multiple types of GABAergic INs are specialized in innervating different subcellular domains of GCs and exert layer- and compartment-specific functions (Freund & Buzsáki, 1996; Halasy & Somogyi, 1993; Hosp et al., 2014; Hsu et al., 2016; Lee et al., 2016; Liu et al., 2014). Soma-targeting INs, such as fast-spiking parvalbumin-expressing (PV<sup>+</sup>) basket cells (BCs), form a dense axonal plexus in the GC layer and provide strong perisomatic inhibition in GCs, thereby controlling action potential (AP) generation (Hu, Gan, & Jonas, 2014; Lee et al., 2016). In contrast, dendrite-targeting INs, such as somatostatin-expressing (SST<sup>+</sup>) hilar perforant path-associated (HIPPA) cells projecting their axons to the outer two-thirds of the molecular layer (ml), regulate dendritic excitability and synaptic plasticity in GCs (Lee et al., 2016; Yuan et al., 2017). In addition to these types, vasoactive intestinal polypeptide-expressing (VIP<sup>+</sup>) INs constitute a major division of cortical INs in parallel with PV<sup>+</sup> and SST<sup>+</sup> INs, representing approximately 30% of the total GABAergic population in the neocortex (Pfeffer, Xue, He, Huang, & Scanziani, 2013; Prönneke et al., 2015; Rudy, Fishell, Lee, & Hjerling-Leffler, 2011; Wall et al., 2016). In the hippocampal CA1 region, distinct VIP<sup>+</sup> IN subtypes have been identified and are thought to modulate hippocampal input–output transformation (Acsády, Görcs, & Freund, 1996; Tyan et al., 2014). Calretinin (CR)-expressing VIP<sup>+</sup> INs mainly inhibit INs, whereas VIP<sup>+</sup> BCs, which coexpress cholecystokinin (CCK), innervate pyramidal cells in the CA1 area (Acsády et al., 1996; Tyan et al., 2014). More recently, a long-range projecting (LRP) type of VIP<sup>+</sup> cells, with axon projecting both locally to the CA1, but also to the subiculum, has been discovered (Francavilla et al., 2018). VIP-LRP neurons show specific molecular properties and target INs within the CA1 area, but both INs and pyramidal cells within the subiculum (Francavilla et al., 2018). Such VIP<sup>+</sup> neuron-mediated disinhibitory circuits in the hippocampal CA1 region are likely to play an active role in supporting goal-oriented spatial learning (Turi et al., 2019).

In the DG, VIP<sup>+</sup> INs have received so far relatively little attention. An early study revealed that VIP<sup>+</sup> neurons in the rat DG exhibit highly diverse morphologies (Hájos, Acsády, & Freund, 1996). However, no attempt has been made to characterize precisely the electrophysiological and synaptic properties of VIP<sup>+</sup> INs in this region due to the difficulty of targeting these neurons. However, an up-to-date Cre mouse driver line for VIP has been generated (Taniguchi et al., 2011), which allows us to address these unanswered questions. In this study, we employed transgenic mice (Madisen et al., 2010; Taniguchi et al., 2011), immunohistochemistry (IHC), electrophysiology, and single-cell reconstruction to investigate the neurochemical, morphological, and intrinsic electrophysiological characteristics of VIP<sup>+</sup> INs in the mouse DG. By combining electrophysiological and optogenetic approaches, we also examined their synaptic connections with different DG neuron types.

## 2 | MATERIALS AND METHODS

### 2.1 | Animals

Transgenic *VIP-Cre* (stock no. 010908; RRID:IMSR\_JAX:010908), *SST-Cre* (stock no. 013044; RRID:IMSR\_JAX:013044), *PV-Cre* (stock no. 008069; RRID:IMSR\_JAX:008069), and *Ai14* (stock no. 007914; RRID:IMSR\_JAX:007914) mouse lines were obtained from Jackson Laboratory (Bar Harbor, ME, USA). By crossing the *VIP-Cre* driver with *Ai14* mice, *VIP-Cre;Ai14* mice with selective tdTomato expression in VIP<sup>+</sup> neurons were generated. Mice of both sexes at postnatal days 30–90 were used for the experiments. All animals were handled in accordance with the national and institutional guidelines and the protocol was approved by the Institutional Animal Care and Use Committee of National Yang-Ming University.

### 2.2 | Characterization of the distribution of tdTomato<sup>+</sup> cells in brain sections

*VIP-Cre;Ai14* mice were perfused with 4% paraformaldehyde (PFA), and coronal, sagittal, or transverse sections of the brain were cut into 60- $\mu$ m sections. Slices were mounted in Vectashield with nuclear stain 4',6-diamidino-2-phenylindole (DAPI; Vector Laboratories, Burlingame, CA, USA). A single plane of tdTomato expression was captured using a stereo microscope equipped with epifluorescent illumination (SZX16, Olympus, Tokyo, Japan).

### 2.3 | Virus and stereotaxic viral injections for optogenetic experiments

To selectively activate VIP<sup>+</sup>, PV<sup>+</sup>, and SST<sup>+</sup> neurons in the DG, we utilized a Cre-inducible channelrhodopsin-2 (ChR2) construct (AAV5-EF1 $\alpha$ -DIO-hChR2(rH134R)-eYFP or AAV9-EF1 $\alpha$ -DIO-hChR2(E123T/T159C)-eYFP) obtained from the University of North Carolina vector core (NC, USA) or Addgene (MA, USA). Mice (postnatal days >45) were anesthetized with 4% (v/v) isoflurane (Halocarbon Laboratories, North Augusta, SC, USA) in 100% oxygen (air flow rate, 4 ml/min) in an induction chamber (Hsu et al., 2016; Lee, Kruglikov, Huang, Fishell, & Rudy, 2013), then the heads were shaved. Mice were placed in the stereotaxic frame (IVM-3000; Scientifica, Uckfield, UK) and kept under a constant flow rate. The mouth and nose of each mouse were immersed into the mask with approximately 1.5% sustained isoflurane air flow. A temperature controller (TMP-5b; Supertech, Pécs, Hungary) was placed below the mice to maintain a constant body temperature (approximately 36°C). After securing the head with two ear bars, 75% ethanol was used to disinfect the surgical area, and the animal's eyes were protected by an ophthalmic gel. To target the DG, a midline scalp incision (approximately 1 cm) was made using scissors and the skin was pulled aside to expose the skull. Small craniotomies (ventral DG, coordinates from Bregma, anteroposterior [AP]: –3.4 mm; mediolateral [ML]:  $\pm$ 2.8 mm; dorsal DG, coordinates from Bregma, AP: 2 mm; ML:  $\pm$ 1.3 mm) were

made bilaterally. The viral vector was delivered through the craniotomy to the two locations within the hippocampus (ventral DG, dorsoventral [DV]: -4.4 and -4.2 mm; dorsal DG, DV: -2 and -1.8 mm) using a 10- $\mu$ l NanoFil syringe (World Precision Instruments, Sarasota, FL, USA) and a 35-G beveled metal needle. The injection volume (.5  $\mu$ l at each location) and flow rate (.1  $\mu$ l/min) were controlled with a nanopump controller (KD Scientific, Holliston, Massachusetts, USA). After injection, the needle was retained for 10 min and then withdrawn slowly and a subcutaneous injection of carprofen (5 mg/kg) or ketorolac (6 mg/kg) was administered as a postoperative analgesic. All animals were allowed at least 3 weeks for complete recovery and viral expression.

## 2.4 | Slice electrophysiology and optical stimulation

Coronal or transverse brain slices of 400  $\mu$ m thickness were prepared from both *VIP-Cre;Ai14* and AAV-infected *VIP-Cre*, *PV-Cre*, and *SST-Cre* mice using a vibratome (DTK-1000; Dosaka, Kyoto, Japan). All animals were sacrificed by decapitation. The brains were rapidly removed and slices were cut in ice-cold cutting saline containing the following (in mM): 87 NaCl, 25 NaHCO<sub>3</sub>, 1.25 NaH<sub>2</sub>PO<sub>4</sub>, 2.5 KCl, 10 glucose, 75 sucrose, .5 CaCl<sub>2</sub>, and 7 MgCl<sub>2</sub>. Brain slices were incubated in oxygenated (95% O<sub>2</sub>, 5% CO<sub>2</sub>) cutting saline for recovery at 34°C and stored at room temperature until used. During experiments, slices were placed in the recording chamber and perfused with oxygenated artificial cerebrospinal fluid (ACSF) containing the following (in mM): 125 NaCl, 25 NaHCO<sub>3</sub>, 1.25 NaH<sub>2</sub>PO<sub>4</sub>, 2.5 KCl, 25 glucose, 2 CaCl<sub>2</sub>, and 1 MgCl<sub>2</sub>.

For the whole-cell recordings, the cells were visually selected under the microscope (BX51WI; Olympus, Japan) equipped with infrared Dodt gradient contrast (IR-DGC) illumination. Recordings were performed with a MultiClamp 700B amplifier (Molecular Devices, Sunnyvale, CA, USA). Recording electrodes (3–5 M $\Omega$ ) were pulled from borosilicate glasses with a filament (outer diameter, 1.5 mm; wall thickness, .32 mm; Harvard Apparatus, Edenbridge, UK). For the measurement of intrinsic properties, glass pipettes were filled with a low Cl<sup>-</sup> internal solution containing the following (in mM): 136.8 K-gluconate, 7.2 KCl, .2 EGTA, 4 MgATP, 10 HEPES, 7 Na<sub>2</sub>-phosphocreatine, .5 Na<sub>3</sub>GTP (pH 7.3 with KOH), and .4% (w/v) biocytin (Life Technologies, Grand Island, NY, USA). In experiments on ChR2-eYFP-expressing neurons, optogenetic-assisted circuit mapping, and paired recording, pipettes were filled with a high Cl<sup>-</sup> internal solution containing (mM): 15 K-gluconate, 140 KCl, .1 EGTA, 2 MgCl<sub>2</sub>, 4 Na<sub>2</sub>ATP, 10 HEPES, .5 Na<sub>3</sub>GTP, and .4% biocytin. For cell-attached recording and subsequent measurement of excitatory (E)-inhibitory (I) conductance ratio following, pipettes were filled with a Cs<sup>+</sup>-based intracellular solution containing the following (in mM): 121.5 CsMeSO<sub>3</sub>, .1 EGTA, 4 MgCl<sub>2</sub>, 13.5 CsCl, 10 HEPES, 5 QX-314 bromide, 2 Na<sub>2</sub>ATP, 10 Na<sub>2</sub>-phosphocreatine, and .3 Na<sub>3</sub>GTP. We also performed a subset of cell-attached recordings using the K-gluconate-based internal solution and found that Cs<sup>+</sup> in the pipette did not alter the firing of recorded neurons in cell-attached mode (unpublished

observation). In most recordings, the pipette capacitance was fully compensated and series resistance was compensated to approximately 80% (Bandwidth: 1–2 kHz) in the voltage-clamp configuration. Signals were low-pass filtered at 4 kHz and sampled at 10 kHz using Digidata 1440A (Molecular Devices). A Digidata 1440A connected to a personal computer was used for stimulus generation and data acquisition. Pulse sequences were generated by pClamp 10.2 (Molecular Devices). All recordings were conducted at 32  $\pm$  1°C, except the experiments of optogenetics, which were performed at 23  $\pm$  2°C for the comparison with our previous study (Hsu et al., 2016).

Cell-attached recording (pipette resistance, 5–6 M $\Omega$ ) was conducted to detect spike during perforant path (PP) stimulation, and an extracellular stimulation electrode (tip diameter, approximately 10  $\mu$ m; filled with ACSF) was used for orthodromic stimulation of the PP. Trains of stimulation with near-threshold intensities at 10 Hz were delivered every 15 s using a stimulus isolator (ISO-flex; A.M.P.I., Jerusalem, Israel). With near-threshold intensities, each train triggered at least one spike in 50% of trials and the probability of spike generation triggered by any stimulus was <.8 (Liu et al., 2014; Pouille & Scanziani, 2004). Antidromic spikes, distinguished by a lack of spike jitter, were excluded.

For optical stimulation, ChR2 was excited by optical stimuli at 470 nm (driven by DC4104, Thorlabs, Newton, NJ, USA), which was delivered directly through the objective. The optical stimuli were simultaneously recorded by a GaP photodiode (wave-length range, 150–550 nm; Thorlabs). Photocurrents recorded from the eYFP-expressing neurons and inhibitory synaptic responses were evoked by 5-Hz trains of photostimulation (light pulse duration, 5 ms; inter-train interval, 15 s). Light intensity was measured using a photometer (5–7 mW in blue light delivering area; Thorlabs).

## 2.5 | Post-hoc morphological reconstruction

To investigate the morphology of the recorded cells (filled intracellularly with .4% biocytin), the slices were fixed overnight with 4% PFA in phosphate-buffered saline (PBS). After washing with PBS three times, slices were incubated with streptavidin-conjugated Alexa Fluor 594 or 488 (1:300; Life Technologies, Grand Island, NY, USA) in PBS and .2% (v/v) Triton X-100 (USB Co., Cleveland, OH, USA) overnight at 4°C. After washing with PBS, they were mounted in Vectashield with DAPI (Vector Laboratories, Burlingame, CA, USA). Labeled neurons were examined using a two-photon microscope with a pulsed titanium:sapphire laser (Chameleon Ultra II tuned to 800 nm for scanning; Coherent, Portland, OR, USA) attached to a Leica DM6000 CFS (Leica Microsystems, Wetzlar, Germany) that was equipped with the 20 $\times$ /1.0 NA water immersion objective (HCX APO L; Leica Microsystems, Wetzlar, Germany). In a subset of experiments, labeled neurons and viral expression were imaged using confocal argon or HeNe laser excitation (Leica Microsystems, Wetzlar, Germany). For single neuron reconstructions, image stacks were imported into the Neuromantic 1.6.3 software (RRID:SCR\_013597). Cells chosen for reconstruction were based on the following criteria: (1) good quality,

complete labeling of the visualized neuron without signs of disintegration (e.g. fading of biocytin signal or formation of blebs in distal dendrites), (2) no major dendrite cut close to the soma, and (3) presence of a substantial collaterization of the axon. Morphological parameters were analyzed using Neurolucida Explorer (MBF Bioscience, Williston, VT, USA; RRID:SCR\_017348). To quantify the axonal distribution, we counted the number of intersections made by the axons with lines running parallel to each layer and interspaced by 10  $\mu\text{m}$  (Liu et al., 2014).

## 2.6 | Chemicals and drugs

To examine the function of ChR2, a sodium channel antagonist tetrodotoxin citrate (TTX, 1  $\mu\text{M}$ ; Ascent Scientific) was used to isolate photocurrents. In experiments of optogenetic-assisted circuit mapping of VIP<sup>+</sup> INs, kynurenic acid (2 mM; Sigma-Aldrich, St. Louis, MO) was utilized to block AMPA/NMDA receptors. In a subset of optogenetic experiments, postsynaptic inhibitory currents were blocked by the GABA<sub>A</sub> receptor blocker SR-95531 (1  $\mu\text{M}$ ; Tocris) and GABA<sub>B</sub> receptor blocker CGP35348 (1  $\mu\text{M}$ ; Tocris).

## 2.7 | Immunohistochemistry (IHC)

For colocalization of neuronal markers, *VIP-Cre;Ai14* mice were perfused with 4% PFA and the brain was postfixed in PFA at 4°C for

2–6 h. The DG was cut into 60  $\mu\text{m}$ , washed in .1% Triton X-100 in Tris-buffered saline (TBS), and incubated in a blocking solution containing 5% normal goat serum (Vector Laboratories, Burlingame, CA, USA) or 1–2X animal-free blocker (Vector Labs, Burlingame, CA, USA) in TBS at 23–25°C for 2–4 h. Slices were then incubated with primary antibodies (Table 1) in the blocking solution at 4°C for 24–48 h, washed in TBS three times for 10 min each, followed by 2–4 h of secondary antibody (Table 2) incubation at 23–25°C, and washed six times in TBS for 10 min each. Slices were mounted in Vectashield with DAPI (Vector Labs, Burlingame, CA, USA). Confocal/two-photon images were acquired sequentially using Leica DM6000 CFS equipped with the 20x/1.0 NA water immersion objective.

## 2.8 | Hierarchical clustering analysis

For cell clustering, we performed squared Euclidean distances and Ward's method (Ward, 1963). All electrophysiological properties of VIP<sup>+</sup> INs were tested using the D'Agostino-Pearson normality test and Pearson's correlation test. Non-independent variables were excluded with an absolute value of a correlation coefficient > .7 (Guerra et al., 2011). In the hierarchical clustering analysis (HCA), each variable was normalized to the z-score. The distance between data points represents the dissimilarity between them, and closer data points have higher similarity. The color keys in the heatmap represent the log<sub>2</sub>-fold z-score change in certain features in individual cells

**TABLE 1** Primary antibodies used in study

Antibody/species	Immunogen	Dilution	Source/catalog/RRID	Reference
VIP (pAb <sup>a</sup> ), rabbit	Porcine VIP coupled to bovine thyroglobulin	1:1000	Immunostar, 20077, AB_572270	Prönneke et al., 2015
CR (mAb <sup>b</sup> ), mouse	Chick retina, specific for an epitope between amino acids 2–27 at the N-terminus of calcitonin	1:300	Santa Cruz, SC-365956, AB_10846469	Wakeham, Ren, & Morgans, 2020
CCK (pAb), rabbit	Synthetic sulfated CCK-8(26–33) amide	1:800	Sigma, C-2581, AB_258806	Tyan et al., 2014
PV (mAb), mouse	Carp-II PV, against PV calcium-binding protein of the EF-hand family	1:500	Swant, 10–11 (F), AB_10000343	Donato, Rompani, & Caroni, 2013
SST (mAb), rat	Synthetic 1–14 cyclic somatostatin conjugated to bovine thyroglobulin using carbodiimide	1:1000	Millipore, MAB354, AB_2255365	Marlin, Mitre, D'amour, Chao, & Froemke, 2015

<sup>a</sup>Polyclonal antibody.

<sup>b</sup>Monoclonal antibody.

Antibody/species	Host	Dilution	Source/catalog/RRID
Alexa Fluor 488 anti-rabbit	Goat	1:500	Invitrogen, A-11008, AB_143165
Alexa Fluor 488 anti-mouse	Goat	1:500	Invitrogen, A-11001, AB_2534069
Alexa Fluor 488 anti-rat	Goat	1:500	Invitrogen, A-11006, AB_141373
Alexa Fluor 594 anti-rat	Goat	1:500	Invitrogen, A-11007, AB_141374
Alexa Fluor 633 anti-mouse	Goat	1:500	Invitrogen, A-21052, AB_2535719

**TABLE 2** Secondary antibodies used in study

compared to other cells. To determine the optimal groups ( $k$ ) of  $k$ -means in electrophysiological clustering, we used the average silhouette method (Rousseeuw, 1987) to compute different values of  $k$ . The number of  $k$  cluster equal to three had the greatest average silhouette width. The analysis was conducted using the free statistic software (ClustVis: a web tool for visualizing clustering of multivariate data, <https://biit.cs.ut.ee/clustvis/>; RRID:SCR\_017133).

## 2.9 | Data analysis and statistics

Data were analyzed using Clampfit 10.6 (Molecular Devices; RRID: SCR\_011323) and Prism 6.0 (GraphPad, La Jolla, CA, USA; RRID: SCR\_002798). AP trains were generated by 1-s current injection (with an increment of 20 pA) with the membrane potential kept at approximately  $-65$  mV. The  $R_{in}$  was calculated by dividing the amplitude of small hyperpolarizing current ( $-10$  pA, 1 s) by the elicited steady-state voltage change. The membrane time constant was measured using a single-exponential fit to the early portion of the voltage change produced by hyperpolarizing current injection ( $-5$  pA). The AP threshold was measured as the voltage at which the first derivative exceeded 20 V/s (Hosp et al., 2014; Hou et al., 2016). The half-width of the AP was measured at two points during the rise and decay phase halfway between the threshold and peak. The after-hyperpolarization potential (AHP) amplitude was defined as the most negative deflection following the peak of AP and measured from the threshold. The maximum rising rate and maximum falling rate were calculated from the AP evoked by the rheobase current (the minimal intensity of the 1-s current pulse required for AP generation) injection and the peak amplitude was measured from the AP threshold. The adaptation (AD) ratio is defined as the peak amplitude of the last spike divided by the first spike. The AD ratio, coefficient of variation of interspike interval (ISI), last spike onset, and mean AP frequency were measured during a 1-s current step (100 pA) injection. To assess the gap junction between VIP INs and other DG neurons, sustained hyperpolarizing current ( $-20$  pA, 1 s) was applied.

Two-tailed Fisher's exact test was used for statistical comparison of the connectivity. Data were presented as mean  $\pm$  standard error of the mean (*SEM*). Error bars in the figures also represent *SEM*. Statistical significance was tested using the Kruskal-Wallis analysis of variance, Mann-Whitney *U*-test, Fisher's exact test, or Pearson's normality test at the significance level (*p*), as indicated using Prism 6.0.

## 3 | RESULTS

### 3.1 | Identification of VIP<sup>+</sup> INs in the mouse DG

To identify VIP<sup>+</sup> INs in the DG, we crossed a *VIP-Cre* driver line with a Cre-dependent reporter *Ai14* to enable the expression of the fluorescent protein tdTomato in these INs (Figure 1(a); Madisen et al., 2010; Taniguchi et al., 2011). To observe the distribution patterns of the tdTomato reporter, we prepared thin (60  $\mu$ m) brain sections (Figure 1

(b)–(e)). In the DG, tdTomato<sup>+</sup> neurons were mostly detected in the hilus (h) and at lower density in the molecular layer (Figure 1(c)–(e)). To test the specificity of VIP expression in tdTomato<sup>+</sup> cells, we performed VIP IHC (Figure 1(f)). On average,  $81.0 \pm 5\%$  of tdTomato<sup>+</sup> cells in the DG were VIP<sup>+</sup> (87/106 cells in 18 slices from two mice), whereas  $87.4 \pm 3.1\%$  of VIP<sup>+</sup> cells in the DG were tdTomato<sup>+</sup> cells (89/101 cells in 18 slices from two mice; Figure 1(g)). Notably, 10–15% of tdTomato<sup>+</sup> cells showed GC-like morphology and were localized in the granule cell layer of the DG (arrowheads in Figure 1(c)–(e)). However, these tdTomato<sup>+</sup> GC-like cells were not VIP-immunoreactive (0/14 cells in 18 slices from two mice; Figure 1(g)).

To characterize neurochemical diversity of VIP<sup>+</sup> INs, we performed additional IHC for the calcium-binding protein calretinin (CR) or neuropeptide cholecystokinin (CCK) (Hájos et al., 1996). On average,  $17.6 \pm 2.5\%$  of VIP<sup>+</sup> INs in the DG (25/141 cells in 25 slices from three mice) were immunoreactive for CR (Figure 1(h)), whereas only  $6.0 \pm 2.4\%$  of VIP<sup>+</sup> INs in the DG (6/69 cells in 30 slices from three mice) were CCK-positive (Figure 1(i)). Furthermore, consistent with a previous report (Hájos et al., 1996), VIP<sup>+</sup> cells in the DG were not PV- or SST-immunoreactive (for PV, 0/80 cells in 14 slices from two mice; Figure 1(j); for SST, 0/42 cells in seven slices from two mice; Figure 1(k)). The specificity of antibodies against different markers was further verified by their colocalization with VIP<sup>+</sup> neurons in the CA1 area (unpublished data) and the results were in line with previous reports (Acscády et al., 1996; Turi et al., 2019; Tyan et al., 2014).

### 3.2 | Morpho-physiological differences between tdTomato<sup>+</sup> GCs and INs

Our IHC results revealed that approximately 10–15% of tdTomato<sup>+</sup> cells displayed GC-like morphology and were not VIP<sup>+</sup>. To examine whether this subset of tdTomato<sup>+</sup> cells were functionally distinct from VIP<sup>+</sup> INs, we characterized electrophysiological properties of all recorded tdTomato<sup>+</sup> cells. We randomly performed whole-cell patch-clamp recording from a sample of 122 tdTomato<sup>+</sup> cells in transverse hippocampal slices under the IR-DGC and epifluorescent microscope (Figure 2(a)). Hyperpolarizing and depolarizing current steps (1 s) were applied to assess their passive and active membrane properties. After recordings, biocytin-filled cells were morphologically reconstructed. The tdTomato<sup>+</sup> INs displayed highly branched local axon arbors compared to the tdTomato<sup>+</sup> GCs (Figure 2(b), (c)). Physiologically, tdTomato<sup>+</sup> INs exhibited more depolarized RMP (IN,  $-47.6 \pm 1$  mV,  $n = 106$  vs. GC,  $-77.1 \pm 1.7$  mV,  $n = 16$ ;  $p < .001$ ), strong AP amplitude adaptation (AD) (IN,  $.32 \pm .02$  vs. GC,  $.88 \pm .02$ ;  $p < .001$ ), lower rheobase (IN,  $16.0 \pm 1.1$  pA vs. GC,  $34.8 \pm 4.5$  pA;  $p < .001$ ), larger  $R_{in}$  (IN,  $915 \pm 37$  M $\Omega$  vs. GC,  $504 \pm 53$  M $\Omega$ ;  $p < .001$ ) relative to tdTomato<sup>+</sup> GCs (Figure 2(d)). In fact, the separation of these tdTomato<sup>+</sup> neurons was so clear that the two parameters, the AD ratio and the RMP, could identify the two non-overlapping clusters (Figure 2(e)). Furthermore, tdTomato<sup>+</sup> INs exhibited a narrower spike half-width (IN,  $.79 \pm .02$  ms vs. GC,  $1.02 \pm .05$  ms;  $p < .001$ ), larger

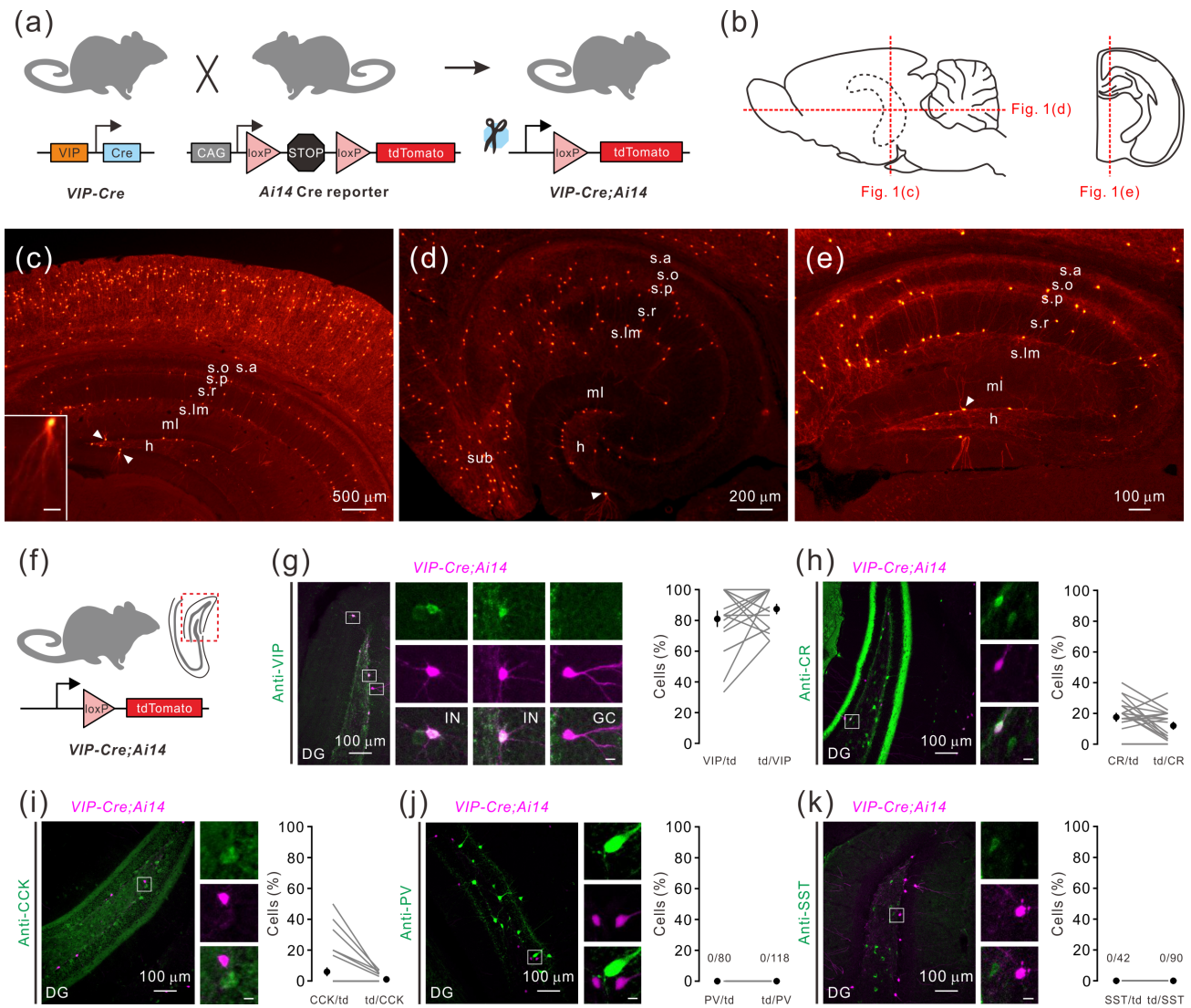


**FIGURE 1** Genetic identification of VIP-expressing neurons in the mouse DG. (a) The mating strategy using a *VIP-Cre* driver and a reporter line to label *VIP*<sup>+</sup> neurons. The *Ai14* Cre reporter mice harbor a loxP-flanked STOP cassette preventing transcription of the CAG promoter-driven tdTomato red fluorescent protein. The Cre recombinase (“scissor”) excises the STOP codon and results in transcription of tdTomato in *VIP-Cre*; *Ai14* mice. (b) Left, diagram of the lateral view of the mouse brain. Red lines indicate the coronal (Fig. 1c) or transverse section (Fig. 1d) cut through one hemisphere, which contained the hippocampus (dotted line). Right, red vertical line indicates the parasagittal section plane (Fig. 1e). (c–e) Distribution of *VIP*<sup>+</sup> neurons in adult *VIP-Cre*; *Ai14* mice. Note that the neurites of *VIP*<sup>+</sup> neurons segregated into distinct laminae in the stratum alveus (s.a), stratum pyramidale (s.p), stratum lacunosum moleculare (s.lm), and hilus (h) of the hippocampus. Arrowheads and enlarged images indicate the GC-like neurons. s.o, stratum oriens; s.r, stratum radiatum; ml, molecular layer. Scale bar in the inset = 50  $\mu$ m. (f) Experimental schematic of IHC with coronal sections of *VIP-Cre*; *Ai14* mice. The box indicates the area (including sections randomly selected from different dorsoventral regions of the DG) for immunofluorescence analyses. (g–k) Confocal image stacks of the immunofluorescence of VIP, CR, CCK, PV, and SST in the DG. High-magnification of boxed areas were shown in the inset. Filled circles represent the average of colocalizations, whereas lines indicate individual quantifications from the same slice. Scale bar = 10  $\mu$ m (enlarged cell). Data are expressed as mean  $\pm$  SEM [Color figure can be viewed at [wileyonlinelibrary.com](http://wileyonlinelibrary.com)]

AHP (IN,  $-17.6 \pm .4$  mV vs. GC,  $-13.7 \pm .6$  mV;  $p < .001$ ), smaller AP peak amplitude (IN,  $56.6 \pm 1.1$  mV vs. GC,  $91 \pm 3.3$  mV;  $p < .001$ ), and faster AP falling rate (IN,  $126.4 \pm 4.6$  V/s vs. GC,  $89.1 \pm 5.5$  V/s;  $p < .001$ ) relative to tdTomato<sup>+</sup> GCs (Table 3). In summary, while tdTomato<sup>+</sup> GC-like neurons exhibited physiological properties similar to those of GCs, the tdTomato<sup>+</sup> INs showed clearly distinct electrophysiological characteristics.

### 3.3 | Morpho-physiological classification of *VIP*<sup>+</sup> INs

*VIP*<sup>+</sup> INs displayed heterogeneous axonal distribution patterns (Figure 3(a)). Based on the location of their axonal projections, *VIP*<sup>+</sup> INs were classified into four subtypes: (1) hilus-projecting (HP) cells (27/40 cells), (2) molecular layer (ml)-projecting (MP) cells (6/40 cells),

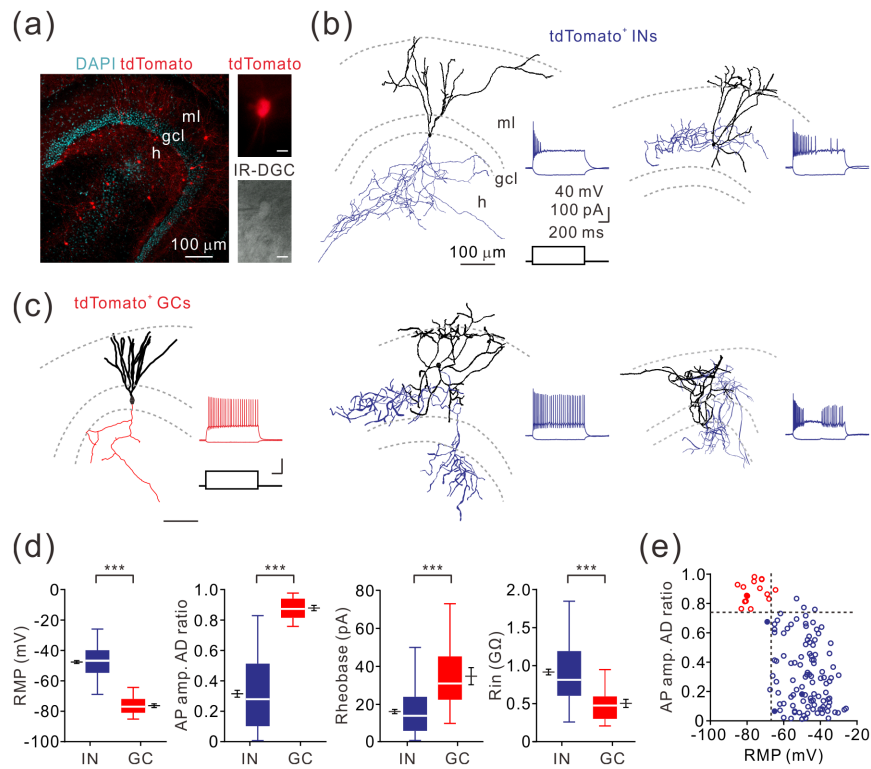


**FIGURE 2** Morpho-physiological differences between tdTomato<sup>+</sup> GCs and INs. (a) Left, two-photon image stacks of tdTomato and nuclear stain 4',6-diamidino-2-phenylindole (DAPI, blue) in the DG. A transverse hippocampal section was obtained from a *VIP-Cre;Ai14* mouse. Right, tdTomato fluorescence (top) and IR-DGC (bottom) images of a recorded cell. gcl, granule cell layer. (b, c) Reconstructed morphologies and membrane responses of tdTomato<sup>+</sup> neurons to current injections. Somata and dendrites of putative INs were in black and the axons were in blue; the soma and dendrites of the GC-like cell were shown in black and the axons were shown in red. (d) Whisker plots of intrinsic properties of resting membrane potential (RMP), action potential (AP) amplitude adaptation (AD) ratio, rheobase, and input resistance ( $R_{in}$ ) of tdTomato<sup>+</sup> INs ( $n = 106$ ) and GCs ( $n = 16$ ). The mean  $\pm$  SEM were represented next to the boxes. \*\*\* $p < .001$ . (e) Scatterplot of AP amplitude AD ratio versus RMP. Red and blue circles represent GC-like cells and putative INs, respectively. Dashed lines indicate the arbitrary cutoff values (AD ratio, .75; RMP,  $-68$  mV) that appropriately differentiate two populations. Filled circles represent neurons shown in (b) and (c) [Color figure can be viewed at [wileyonlinelibrary.com](http://wileyonlinelibrary.com)]

(3) bistratified (Bis) cells (4/40 cells), and (4) trilaminar (Tri) cells (3/40 cells) (Figure 3(a); Table 4). The axon of the HP cells arborized profusely in the hilus. The MP cells projected their axon preferentially to the inner two-thirds of the ML. The Bis cells had a unique axonal pattern with two separate axon collateral clusters located in the inner ML (IML) and hilus, whereas the Tri cells had wide axonal branches across the three layers, the IML, granule cell layer (GCL or gcl), and hilus. These four subtypes of VIP<sup>+</sup> INs also differed in their somatic locations. The HP cells were mostly located in the hilus (20/27), whereas the other VIP<sup>+</sup> IN subtypes were primarily located in the ML (Figure 3 (b); MP, 5/6 cells, Bis, 4/4 cells, and Tri, 3/3 cells).

VIP<sup>+</sup> INs exhibited variable discharge patterns in response to 1-s depolarizing current steps of injection. First, we divided them into three phenomenological subtypes based on their discharge patterns: fast-adapting (FAD), regular spiking (RS), and irregular spiking (IRS; Figure 3(c)). In 106 recorded cells, VIP<sup>+</sup> INs predominantly exhibited FAD firing pattern (50/106 total cells). Next, we performed an unbiased hierarchical cluster analysis based on electrophysiological properties of all VIP<sup>+</sup> INs (see Materials and Methods for the details) and identified three major classes designated as A, B, and C (Figure 3(c);

Table 5). Correlating VIP<sup>+</sup> IN physiological subtypes defined by the two approaches, we found that electrophysiologically defined classes A, B, and C were mainly FAD, RS, and IRS, respectively (Figure 3(d)). Comparison of morphologically defined IN subtypes showed that while there was some heterogeneity in some electrophysiological features (Table 6), most morphological VIP<sup>+</sup> IN subtypes showed weak correlations with electrophysiologically defined classes (Figure 3(d)). Note, in particular, that all Tri cells were classified as class C and exhibited IRS patterns, indicating a level of association between morphological and electrophysiological features (Hosp et al., 2014).

Finally, these four types of VIP<sup>+</sup> INs also displayed diverse and variable dendritic patterns (Figure 4). The dendrites of the HP cells were predominantly located in the ML with variable complexities (Figure 4(a)). Notably, some of HP cells located in the IML and exhibited semilunar GC-like (SGCs) morphologies, for example, the first and third cells from left in the second row as well as the first cell in the fourth row. These three neurons had multiple (>3) primary dendrites and showed wide dendritic morphology. However, unlike classical SGCs, they had high input resistance and more depolarized resting

**TABLE 3** Electrophysiological properties of tdTomato<sup>+</sup> GCs and INs in the DG

	GC (16)	IN (106)	<i>p</i> <sup>a</sup>
AP amplitude AD ratio	.88 ± .02	.32 ± .02	<.001
CV of ISI	.30 ± .03	.52 ± .04	.32
Mean AP frequency (Hz)	17.3 ± 2.0	22.4 ± 2.1	.69
Last AP onset (ms)	956.3 ± 7.4	564.3 ± 39.2	.003
Threshold (mV)	−34.2 ± 1.7	−36.1 ± .6	.46
1st AP max falling rate (V/s)	89.1 ± 5.5	126.4 ± 4.6	<.001
Half-width (ms)	1.02 ± .19	.79 ± .02	<.001
1st AP max rising rate (V/s)	375.1 ± 31.8	278.6 ± 8.9	.002
Max AP frequency (Hz)	39.9 ± 3.3	30.6 ± 2.2	.004
AP peak amplitude (mV)	90.9 ± 3.3	75.6 ± 1.1	<.001
Min/max ISI ratio	.27 ± .04	.35 ± .02	.45
Rheobase (pA)	34.8 ± 4.5	16.0 ± 1.1	<.001
<i>R</i> <sub>in</sub> (MΩ)	503.5 ± 53.0	915.6 ± 37.3	<.001
Rising τ (ms)	48.3 ± 4.5	52.9 ± 2.5	.93
RMP (mV)	−77.1 ± 1.7	−47.6 ± 1.0	<.001
AHP (mV)	−13.7 ± .6	−17.6 ± .4	<.001

Note: Numbers of cells are given in parentheses. All values are provided as mean ± SEM.

<sup>a</sup>*p*-value was examined using Mann–Whitney unpaired *U*-test.

potential (Gupta, Elgammal, Proddatur, Shah, & Santhakuma, 2012). The MP cells projected their dendrites perpendicular to the GCL borders (Figure 4(b)). Dendrites of MP cells were relatively sparse and were mostly distributed to both the ML and hilus. Interestingly, all reconstructed Bis cells extended their dendrites to the subiculum (Figure 4(c)). Of note, dendrites of the Tri cells were highly branched and randomly oriented as compared to those of the Bis cells (Figure 4(c), (d)).

### 3.4 | Delayed recruitment of VIP<sup>+</sup> INs by cortical afferents

DG neurons receive coherent theta (4–10 Hz)-band excitatory inputs *in vivo*, predominantly relayed from the entorhinal cortex (Pernía-Andrade & Jonas, 2014). To assess the recruitment of VIP<sup>+</sup> INs in response to cortical inputs, we stimulated the perforant path fibers by placing a stimulation electrode in the subiculum (sub) close to the hippocampal fissure. While stimulating, we detected the action currents (“spikes”) from individual VIP<sup>+</sup> INs under the cell-attached configuration (Figure 5(a)). To mimic the physiological condition, trains of 10 electrical stimuli were delivered at 10 Hz to the PP. Notably, most VIP<sup>+</sup> INs did not respond to the initial stimuli, but increased their firing probability to latter stimuli during train stimulation (Figure 5(b), (c)).

To probe this late-onset of VIP<sup>+</sup> INs in response to cortical theta inputs, we compared the synaptic inhibitory drive across different levels of excitatory drive by converting currents to conductances, that is, inhibitory postsynaptic conductance (IPSG) versus excitatory

postsynaptic conductance (EPSP). To isolate IPSCs, we used a cesium-based internal pipette solution under the voltage-clamp mode while recording at the reversal potential (0 mV) of AMPA/NMDA receptors. In contrast, EPSCs were recorded at the reversal potential (−50 mV) of GABA<sub>A</sub> receptors. The depression of IPSG but facilitation of EPSP resulted in increasing E/I ratios (Figure 5(d)–(f)).

### 3.5 | VIP<sup>+</sup> INs preferentially innervate DG INs

To investigate the connectivity between VIP<sup>+</sup> INs and DG cells, we performed paired recordings from VIP<sup>+</sup> INs and DG cells (Figure 6(a)). The connectivity between two VIP<sup>+</sup> INs within a distance of approximately 100 μm appeared to be very low as we could only obtain recordings from one synaptically coupled pair in 29 paired recordings. The presynaptic VIP<sup>+</sup> IN was classified as a Tri cell, whereas the postsynaptic VIP<sup>+</sup> IN was classified as a MP cell (Figure 6(a)left, middle, and right). In this pair, the unitary inhibitory postsynaptic current (uIPSC<sub>1</sub>) had an amplitude of 32.9 ± 7.2 pA (average of seven trials). Notably, no reciprocal connections or gap junction coupling were detected between these two cells (see Materials and Methods). Next, we tested reciprocal connections between VIP<sup>+</sup> INs and non-VIP<sup>+</sup> cells, including non-VIP INs, MCs, and GCs. Of 28 pairs, no connection was detected between presynaptic VIP<sup>+</sup> INs and postsynaptic non-VIP cells (Figure 6(a), left and right). Conversely, we detected a non-VIP<sup>+</sup> cell–VIP<sup>+</sup> IN cell pair, in which a total molecular layer (TML)-like cell showed functional coupling onto a HP-VIP<sup>+</sup> IN (Figure 6(a), right, left, and middle; uIPSC<sub>1</sub>, 132.1 ± 10 pA, average of 40 trials). Collectively, VIP<sup>+</sup> INs appeared to form sparse connections with DG cells.

To systematically map the postsynaptic target cells, we employed optogenetic stimulation to activate a population of VIP<sup>+</sup> INs and recorded postsynaptic responses in different types of DG neurons. To this end, the light-sensitive cation channel ChR2 was virally expressed in the dorsal or ventral DG of VIP-Cre mice (Figure 6(b)). Consistent with the tdTomato expression pattern (Figure 1(c)–(e)), ChR2-eYFP signals were predominantly observed in the hilus (Figure 6(c)). In whole-cell recordings, all putative eYFP<sup>+</sup> INs (8/8 cells) generated inward currents and APs in response to a train of short light pulses at 5 Hz (Figure 6(b)). Light-evoked responses were only detected in two of nine eYFP<sup>+</sup> GCs (unpublished data). Therefore, an ionotropic glutamatergic receptor blocker, kynurenic acid (2 mM), was applied to isolate VIP<sup>+</sup> IN-mediated inhibitory transmission.

Next, we recorded IPSCs from different cell types in the DG. Based on their morphological features, six different GABAergic IN subtypes and two types of glutamatergic PNs were classified (Figure 6(d); Table 7). INs were identified by the distribution of their local axon. Both axo-axonic cells (AACs) and BCs had axon largely restricted within the GCL. AACs showed prominent radial axon collaterals, thus also termed chandelier cells, whereas PV BCs have tangential axonal collaterals in the GCL. The axonal arborization of hilar commissural-associational pathway-associated (HICAP)-like cells was mainly confined to the IML. HIPP-like cells projected their axons primarily to the middle and outer ML, whereas TML-like cells project

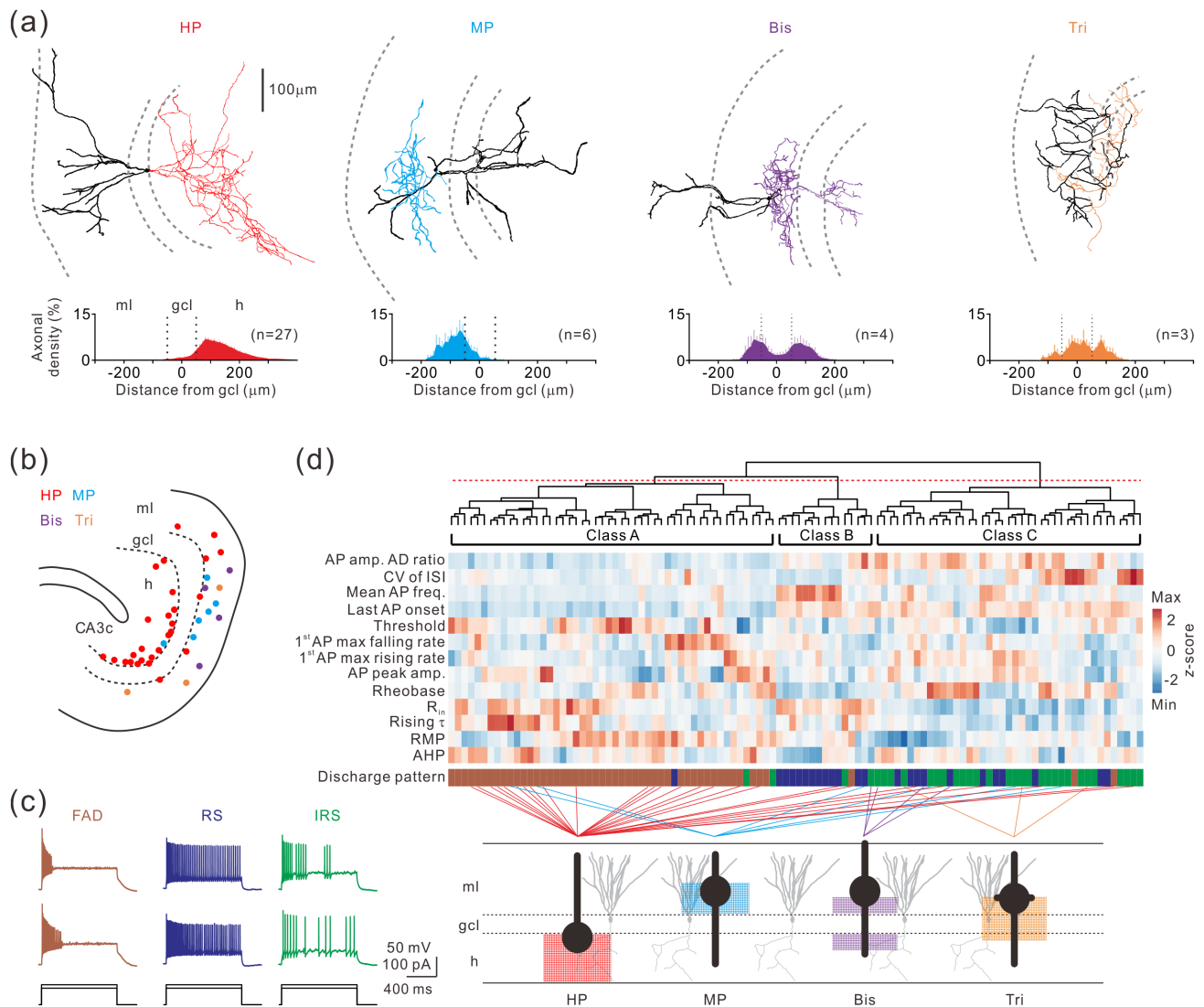


**FIGURE 3** Morpho-physiological classification of VIP<sup>+</sup> INs. (a) Top, exemplar reconstructions of a hilus-projecting (HP) cell with axonal projections to the hilus; molecular layer-projecting (MP) cell with axonal distributions in the inner two-thirds of the molecular layer; bistratified (Bis) cell with axonal plexus distributed in the inner one-third of the molecular layer and hilus; trilaminar (Tri) cell with axonal arborization across the three layers. Somata and dendrites were in black. Axons of HP, MP, Bis and Tri cells were in red, blue, purple, and orange, respectively. Bottom, normalized axonal density across different DG layers. (b) Somatic locations of all reconstructed cells. (c) Exemplar discharge patterns recorded from fast-adapting (FAD, brown), regular spiking (RS, blue), and irregular spiking (IRS, green) VIP<sup>+</sup> INs. The FAD, RS, and IRS types were arbitrarily determined by spiking patterns. (d) Top, hierarchical cluster analysis (HCA) of VIP<sup>+</sup> INs based on their electrophysiological properties. The horizontal-axis of the dendrogram represented the individual cells and the vertical-axis represented the normalized distance (squared Euclidean, Ward's method) between populations (i.e., A, B, C classes). The dashed line was determined by the result of K-means, which was calculated by Silhouette analysis. The heatmap represents the z-score change of each parameter of individual cells (see Materials and Methods section). Bottom, relationship between the electrophysiologically determined cell types and morphologically determined cell types. Color codes below the dendrogram represent FAD (brown), RS (blue), and IRS (green) cells [Color figure can be viewed at [wileyonlinelibrary.com](http://wileyonlinelibrary.com)]

their axon collaterals throughout the entire ML. Hilar-INs were identified by their somata and neurites mainly located in the hilus. ML INs with their soma in the ML can be subdivided into molecular layer perforant path-associated (MOPP) cells and neurogliaform cells (NGFCs) according to their neurochemical, morphological, and physiological properties (Armstrong et al., 2011; Lee et al., 2016). In our experiments, MOPP cells were identified by their larger branching dendritic structure, whereas NGFCs displayed smaller dendritic trees and exhibited late firing patterns

in response to suprathreshold current injection. For glutamatergic PNs, MCs were identified by the large somatic size, their dendrites in the hilus, and the presence of thorny excrescences on their proximal dendrites and somata (Scharfman & Myers, 2013). GCs were distinguished by their dendrites in the ML, their axon with characteristics of mossy fibers, and their relatively hyperpolarized RMP.

Quantification of our results showed that VIP<sup>+</sup> INs preferentially innervated INs over glutamatergic PNs (Figure 6(e), filled bar, IN,

	HP (27)	MP (6)	Bis (4)	Tri (3)	<i>p</i> <sup>a</sup>
<b>Soma</b>					
Perimeter (μm)	36.6 ± 1.2	38.8 ± 3.6	44.2 ± 3.3	37.5 ± 2.4	.334
Major axis (μm)	12.2 ± .3	12.5 ± .9	14.9 ± .7	12.8 ± .2	.085
Minor axis (μm)	9.1 ± .4	9.5 ± 1.2	11.3 ± 1.3	8.7 ± .6	.436
<b>Axons</b>					
Total length (mm)	4.3 ± .4	3.2 ± .2	6.0 ± .3	3.7 ± 1.3	.19
Total surface (mm <sup>2</sup> )	.28 ± .04	.25 ± .04	.42 ± .05	.24 ± .07	.19
NABP <sup>b</sup>	49.6 ± 5.7	37.7 ± 3.8	81.8 ± 4.4	44.7 ± 13.6	.07
ASD1 <sup>c</sup> (mm)	1.0 ± .2	.9 ± .2	1.7 ± .5	1.3 ± .4	.38
ASD2 (mm)	1.9 ± .1	1.6 ± .2	2.1 ± .2	1.3 ± .2	.24
ASD3 (mm)	1.1 ± .2	.7 ± .2	1.5 ± .2	1.0 ± .5	.42
ASD4 (mm)	.43 ± .12	.21 ± .08	.65 ± .30	.23 ± .22	.55
ASD5 (mm)	.12 ± .04	.09 ± .06	.05 ± .05	0	.76
ASD6 (mm)	.03 ± .02	.07 ± .07	0	0	.75
ML 100–200 μm (%)	0	3.9 ± 2.8	0	0	.009
ML 0–100 μm (%)	.3 ± .2	69.2 ± 7.3	15.2 ± 2.8	13.0 ± 5.2	<.001
GCL (%)	8.4 ± 2.4	25.6 ± 9.1	38.6 ± 5.9	50.4 ± 8.2	.01
H 0–100 μm (%)	55.7 ± 3.6	1.3 ± 1.3	44.0 ± 5.2	34.9 ± 7.9	<.001
H 100–200 μm (%)	29.6 ± 3.7	0	2.2 ± 1.0	1.7 ± 1.1	<.001
H 200–300 μm (%)	5.5 ± 1.3	0	0	0	.006
H 300–400 μm (%)	.5 ± .3	0	0	0	.34
<b>Dendrites</b>					
Total length (mm)	2.8 ± .2	2.7 ± .3	2.9 ± .4	3.9 ± .2	.21
Total surface (mm <sup>2</sup> )	.20 ± .03	.19 ± .04	.19 ± .03	.22 ± .01	.54
NDBP <sup>b</sup>	21.4 ± 2.1	20.2 ± 4.6	32.3 ± 4.4	34 ± 4.9	.06
DSD1 <sup>c</sup> (mm)	.6 ± .1	.6 ± .1	.9 ± .2	1.3 ± .2	.06
DSD2 (mm)	1.0 ± .1	.9 ± .1	1.3 ± .4	2.0 ± .3	.1
DSD3 (mm)	.7 ± .1	.7 ± .1	.6 ± .3	.5 ± .2	.79
DSD4 (mm)	.3 ± .1	.3 ± .1	.2 ± .1	.1 ± .1	.83
DSD5 (mm)	.08 ± .04	.10 ± .07	0	0	.35

Note: The numbers indicate every 100 μm as an interval. For example, DSD1 represented the dendrite length within 0–100 μm far from the soma location. The numbers of cells were provided in parentheses. All values were expressed as mean ± SEM.

<sup>a</sup>*p*-value was examined using Kruskal-Wallis unpaired analysis of variance.

<sup>b</sup>NABP and NDBP were short for number of axonal and dendritic branch points, respectively.

<sup>c</sup>ASD and DSD were short for axonal Sholl distance and dendritic Sholl distance, respectively, and were analyzed by NeuroLucida Explorer.

**TABLE 4** Morphological parameters of vasoactive intestinal polypeptide-expressing interneurons

56/97 vs. PN, 5/64; *p* < .001; two-tailed Fisher's exact test). By analyzing neurons that received light-evoked responses, the results showed a large degree of variation in inhibitory postsynaptic conductance (IPSG) within a given cell type and between subtypes (Figure 6 (f)). The connectivity of VIP<sup>+</sup> INs to GCs was low (6.5%; 3/46 cells). Interestingly, two of these three GCs, which receive monosynaptic inputs from VIP<sup>+</sup> INs, were located at the outer GCL. They had multiple (> 3) primary dendrites and were likely to be SGCs.

Finally, we further confirmed that output synapses of VIP<sup>+</sup> INs were different from those of other INs. To this end, we performed similar experiments using PV-Cre and SST-Cre mice. Similar to our

previous report (Lee et al., 2016), strong eYFP signals in slices from PV-Cre mice were exclusively detected in the GCL (Figure 3(a), (b)), whereas intense eYFP signals in the outer-third and the middle-third of the ML and in the hilus were observed in slices from SST-Cre mice (Figure 3(d), (e)). The expression of Chr2-eYFP was functional because delivery of blue light rapidly evoked IPSCs in GCs (Figure 3 (c), (f)). Notably, the connectivity and synaptic strength of the VIP<sup>+</sup> IN-GC connections were remarkably less than those of PV<sup>+</sup> IN-GC and SST<sup>+</sup> IN-GC connections in the DG (Figure 7(g), (h)). In summary, our results suggest that compared to other major types of INs, VIP<sup>+</sup> INs engage in DG microcircuits with a primary disinhibitory function.

**TABLE 5** Electrophysiological properties of hierarchical clustering analysis-classified vasoactive intestinal polypeptide-expressing interneurons

	A (50)	B (15)	C (41)	<i>p</i> <sup>a</sup>
AP amplitude AD ratio	.13 ± .01	.43 ± .05	.50 ± .03	<.001
CV of ISI	.33 ± .04	.30 ± .06	.82 ± .09	<.001
Mean AP frequency (Hz)	10.6 ± 1.2	51.4 ± 7.7	26.1 ± 2.7	<.001
Last AP onset (ms)	187.6 ± 26.4	937.2 ± 30.8	887.3 ± 32.3	<.001
Threshold (mV)	-35.6 ± .9	-37.1 ± 1.0	-36.5 ± .8	.69
First AP max falling rate (V/s)	123.7 ± 7.6	130.9 ± 13.4	127.9 ± 5.7	.48
Half-width (ms)	.82 ± .03	.76 ± .05	.76 ± .02	.4
First AP max rising rate (V/s)	57.3 ± 4.2	62.6 ± 6.6	43.9 ± 2.4	.02
Max AP frequency (Hz)	21.3 ± 1.5	57.7 ± 8.6	32.1 ± 3.3	<.001
AP peak amplitude (mV)	73.8 ± 1.7	75.3 ± 2.1	78.0 ± 1.5	.33
Min/max ISI ratio	.49 ± .03	.35 ± .06	.17 ± .03	<.001
Rheobase (pA)	13.5 ± 1.2	6.0 ± .8	22.7 ± 2.0	<.001
R <sub>in</sub> (MΩ)	964.8 ± 46.5	1442 ± 80.9	663.3 ± 34.3	<.001
Rising τ (ms)	57.3 ± 4.2	62.6 ± 6.6	43.9 ± 2.4	.02
RMP (mV)	-44.9 ± 1.5	-45.9 ± 2.1	-51.6 ± 1.5	.006
AHP (mV)	-17.4 ± .6	-21.5 ± 1.3	-16.5 ± .7	.003

Note: The numbers of cells were provided in parentheses. All values were expressed as mean ± SEM.  
<sup>a</sup>*p*-value was examined using Kruskal-Wallis unpaired analysis of variance.

**TABLE 6** Electrophysiological properties of morphological-defined vasoactive intestinal polypeptide-expressing interneurons

	HP (27)	MP (6)	Bis (4)	Tri (3)	<i>p</i> <sup>a</sup>
AP amplitude AD ratio	.23 ± .04	.50 ± .10	.60 ± .07	.38 ± .07	.006
CV of ISI	.43 ± .08	.85 ± .16	.54 ± .14	.66 ± .19	.01
Mean AP frequency (Hz)	16.2 ± 2.4	10.3 ± 3.0	25.3 ± 2.5	31.0 ± 3.6	.035
Last AP onset (ms)	421.7 ± 72.3	632.6 ± 128.5	979.0 ± 15.2	974.4 ± 12.2	.01
Threshold (mV)	-36.2 ± 1.0	-37.3 ± 1.6	-37.9 ± 2.5	-38.6 ± 3.0	.82
First AP max falling rate (V/s)	119.7 ± 10.3	96.1 ± 11.5	103.3 ± 30.2	113.8 ± 10.2	.5
Half-width (ms)	.88 ± .04	1.04 ± .11	.91 ± .11	.80 ± .02	.35
First AP max rising rate (V/s)	259.6 ± 16.3	276.5 ± 35.5	303.5 ± 39.8	311.4 ± 25.0	.29
Max AP frequency (Hz)	25.2 ± 2.5	12.2 ± 3.2	30.3 ± 4.9	36.3 ± 3.8	.02
AP peak amplitude (mV)	71.6 ± 2.3	82.9 ± 3.9	75.7 ± 3.2	74.4 ± 3.2	.23
Min/max ISI ratio	.40 ± .04	.11 ± .03	.18 ± .07	.11 ± .04	.002
Rheobase (pA)	15.5 ± 1.9	15.5 ± 5.0	17.8 ± 5.3	21.7 ± 3.8	.55
R <sub>in</sub> (MΩ)	889 ± 73	1089 ± 178	812 ± 155	703 ± 116	.56
Rising τ (ms)	67.5 ± 5.9	69.8 ± 14.3	47.8 ± 1.2	57.7 ± 5.1	.45
RMP (mV)	-47.5 ± 2.2	-49.3 ± 2.7	-60.8 ± 3.8	-53 ± 6.6	.16
AHP (mV)	-16.4 ± .9	-19.4 ± 2.3	-17.2 ± 2.0	-17.1 ± .4	.56

Note: The numbers of cells were provided in parentheses. All values were expressed as mean ± SEM.  
<sup>a</sup>*p*-value was examined using Kruskal-Wallis unpaired analysis of variance.

## 4 | DISCUSSION

In this study, we characterized the neurochemical, morphological, and physiological properties as well as the output connectivity of VIP<sup>+</sup> INs in the mouse DG. We demonstrate that VIP<sup>+</sup> INs comprise four morphologically distinct subtypes with variable physiological properties and preferentially innervate GABAergic INs over glutamatergic PNs.

### 4.1 | Reliable Cre-driver line for the identification of VIP<sup>+</sup> INs in the mouse DG

Due to their low abundance, transgenic approaches are required for selective and efficient targeting or manipulation of the VIP<sup>+</sup> INs in the mouse brain. Although an up-to-date Cre driver line for VIP has been available (Taniguchi et al., 2011), the specificity and sensitivity of this

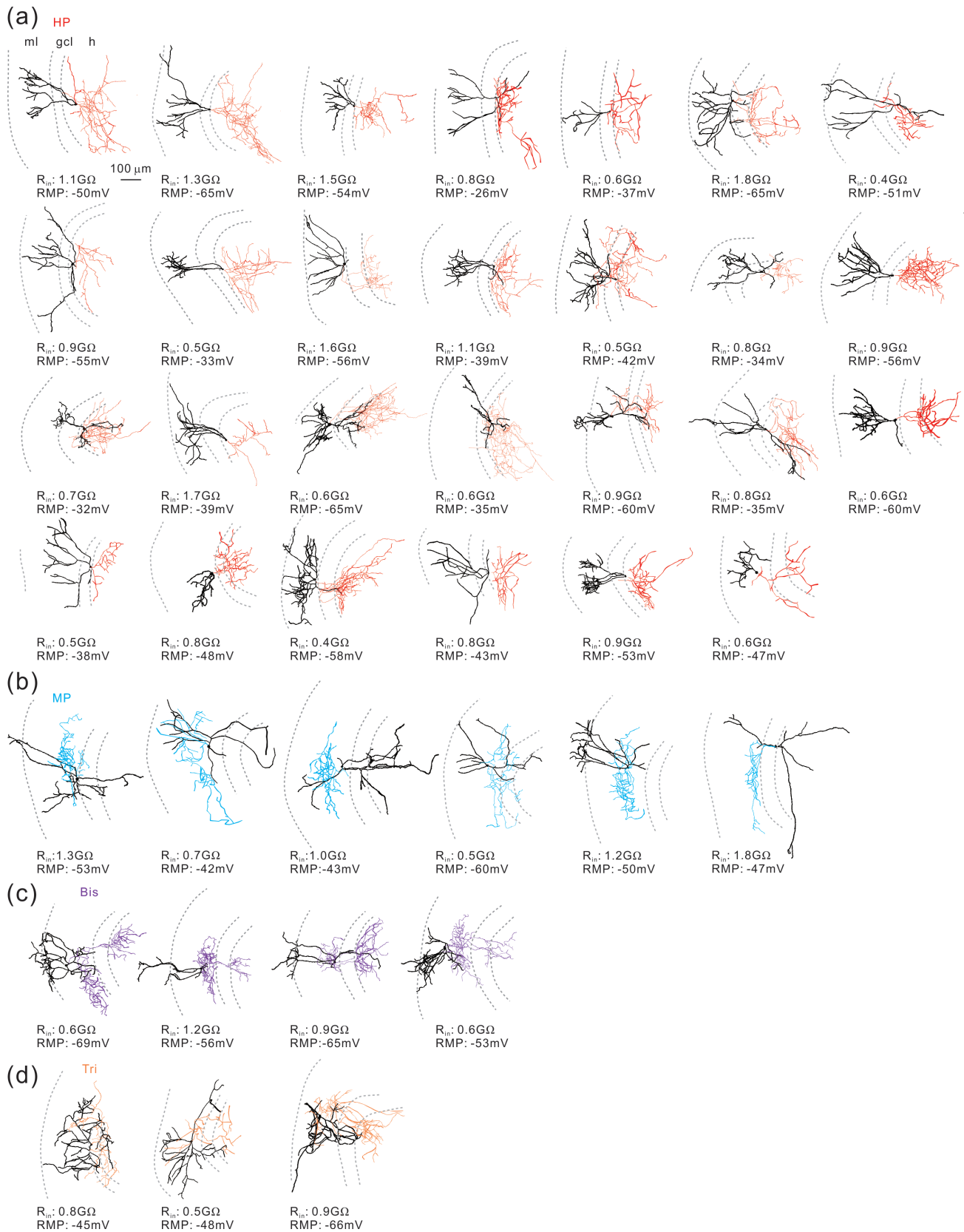
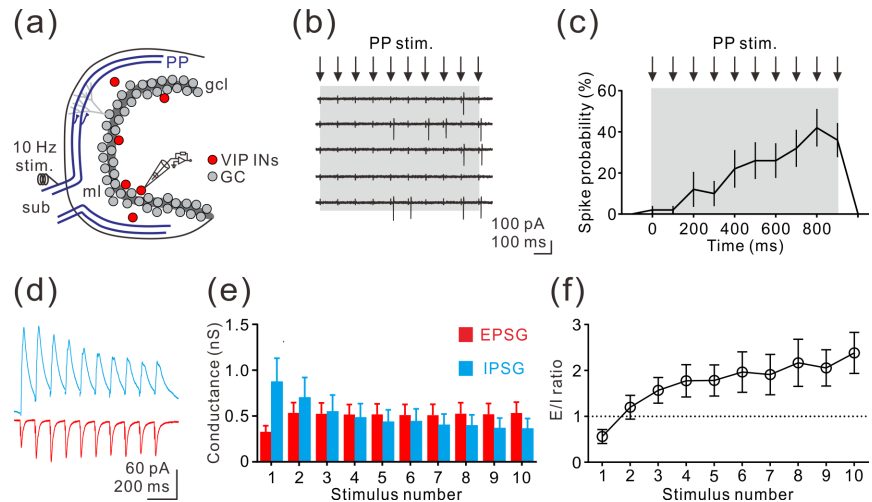


**FIGURE 4** Morphological reconstructions of the DG VIP<sup>+</sup> INs. (a–d) All of the 40 reconstructed VIP<sup>+</sup> INs. The dendrites were depicted in black, and the axons were shown in the same color codes as in Figure 3(a). Values of  $R_{in}$  and RMP were shown below the cell [Color figure can be viewed at [wileyonlinelibrary.com](http://wileyonlinelibrary.com)]

**FIGURE 5** Delayed recruitment of VIP<sup>+</sup> INs by cortical afferents. (a) Experimental schematic. (b) Exemplar cell-attached recording of responses to electrical stimulation with near-threshold intensities delivered at 10 Hz. (c) Histogram showing spike probability of VIP<sup>+</sup> INs in response to perforant path (PP) stimulation ( $n = 15$ ). (d) EPSCs (red,  $V_{\text{hold}} = -50$  mV) and IPSCs (blue,  $V_{\text{hold}} = 0$  mV) evoked by 10-Hz PP stimulation. (e) Summary of EPSCs and IPSCs during 10-Hz stimulation of PP ( $n = 9$ ). (f) Summary of the E/I ratio versus stimulus number during 10-Hz stimulation of PP ( $n = 9$ ). The balanced E/I ratio is indicated by the dashed line [Color figure can be viewed at [wileyonlinelibrary.com](http://wileyonlinelibrary.com)]



line for VIP<sup>+</sup> INs in the DG has remained unclear. In this study, we quantified the co-expression of Cre-driven tdTomato protein with VIP immunofluorescence in the hippocampal CA1 and DG. We found a high degree of overlap between tdTomato<sup>+</sup> and VIP immunoreactive cells in the CA1 (approximately 90%), and a slightly lower degree of convergence in the DG (approximately 80%). Interestingly, a small population of tdTomato<sup>+</sup> GCs (10–15% of the tdTomato<sup>+</sup> population) was also detected in the DG, despite the clear VIP immunonegativity of these neurons. A similar finding was reported in the same mouse line crossed with *Ai9* reporter mice (Taniguchi et al., 2011). In addition, we also observed that a small fraction (two out of nine) of viral-labeled GCs exhibits photocurrents, which may argue against transient VIP expression during development. It is possible that a low level of VIP expression in a small subpopulation of GCs may not be detectable using IHC, whereas efficient Cre/loxP-mediated recombination driven by strong promoters (e.g. CAG or EF1 $\alpha$  in our study) may account for strong tdTomato expression. To circumvent this potential drawback of optogenetic control of VIP<sup>+</sup> INs in behavioral studies, an intersectional strategy that combines two recombination approaches will be required in future studies (Fenno et al., 2014; Taniguchi et al., 2011). For example, the *Dlx5/6-Flp* driver expresses the Flp recombinase in cortical GABAergic neurons (Miyoshi et al., 2010). Accordingly, the use of *VIP-Cre;Dlx5/6-Flp* mouse line may allow specific mapping of VIP<sup>+</sup> INs and selective control of VIP<sup>+</sup> INs.

## 4.2 | DG VIP<sup>+</sup> INs displaying unique neurochemical and cellular features

Consistent with previous reports (Hájos et al., 1996), tdTomato<sup>+</sup> INs did not show any overlap with the two major IN markers, PV and SST, which are corresponding to soma- and dendrite-targeting IN types, respectively. Approximately 20% of VIP<sup>+</sup> INs in the rat DG are CCK immunoreactive and exhibit a BC-like morphology (Hájos et al., 1996). In contrast, we observed a much lower overlap of CCK with tdTomato in the mouse DG and did not detect any VIP<sup>+</sup> INs with their axonal plexus restricted in the GCL. Species differences are likely to account for this discrepancy.

Previous studies reported that CR<sup>+</sup> INs are specialized to control other INs in the rat hippocampus (Gulyás, Hájos, & Freund, 1996; Hájos et al., 1996). Our IHC results showed that CR<sup>+</sup> VIP<sup>+</sup> INs were mostly detected in the subgranular zone of the DG (Figure 1(h)). In agreement with it, we found that CR<sup>+</sup> VIP<sup>+</sup> INs were found mostly (8/9 cells) to be HP cells and most of them (6/9 cells) possessed the FAD discharge pattern (unpublished data). In our CR immunostaining, more abundant CR<sup>+</sup> cells were detected in the ventral hilus compared to the dorsal hilus. This observation was in agreement with previous studies (Liu, Fujise, & Kosaka, 1996; Scharfman & Myers, 2013). Because the CR signal was not detected in dorsal MCs, intense CR expression in the dorsal IML was attributed to the longitudinal axonal projections from ventral MCs, which express CR.

## 4.3 | Morphologically defined VIP<sup>+</sup> INs displaying variable electrophysiological characteristics

VIP<sup>+</sup> INs also display rich diversity in terms of their physiological properties, including discharge pattern. The majority of VIP<sup>+</sup> INs (approximately 45%) exhibit strong AP amplitude AD. Additionally, DG VIP<sup>+</sup> INs showed several unique cellular properties, including small soma size and a corresponding high  $R_{\text{in}}$  (approximately .9 G $\Omega$ ), and a depolarized RMP (approximately  $-48$  mV). The linkages between morphological and physiological profiles of GABAergic INs have been widely investigated in the DG (Hefft & Jonas, 2005; Hosp et al., 2014; Liu et al., 2014). Based on our results, those physiologically defined VIP<sup>+</sup> INs are not remarkably associated with their distinct axonal patterns, indicating that INs cannot be unequivocally classified solely based on electrophysiological or morphological properties. Nevertheless, correlations are shown to exist between these properties and the gene or neurochemical markers (Lien, Martina, Schultz, Ehmke, & Jonas, 2002; Mardinly et al., 2016; Martina, Schultz, Ehmke, Monyer, & Jonas, 1998; Yu, Swietek, Proddutur, & Santhakumar, 2015). Collectively, our data provide novel insight into a hitherto well-known, but poorly characterized, neuronal population in the mouse DG.

### 4.4 | Potential roles of VIP<sup>+</sup> INs in DG networks and behavior

INs receive multiple excitatory afferents from different brain regions and shape the temporal dynamics of the hippocampal network (Hsu et al., 2016; Lee et al., 2016; Liu et al., 2014; Pouille & Scanziani, 2004). Here, we showed that VIP<sup>+</sup> INs receive synaptic currents, which exhibit

facilitating EPSCs and depressing IPSCs in response to theta-band cortical activity. Furthermore, VIP<sup>+</sup> INs have high input resistance (approximately .9 GΩ) and thereby exhibit robust temporal summation in response to 10-Hz perforant path stimulation. Such strong temporal summation suggests that VIP<sup>+</sup> INs may serve as a synaptic integrator and provide long-lasting disinhibition by inhibiting diverse DG IN types during persistent corticohippocampal information flow.

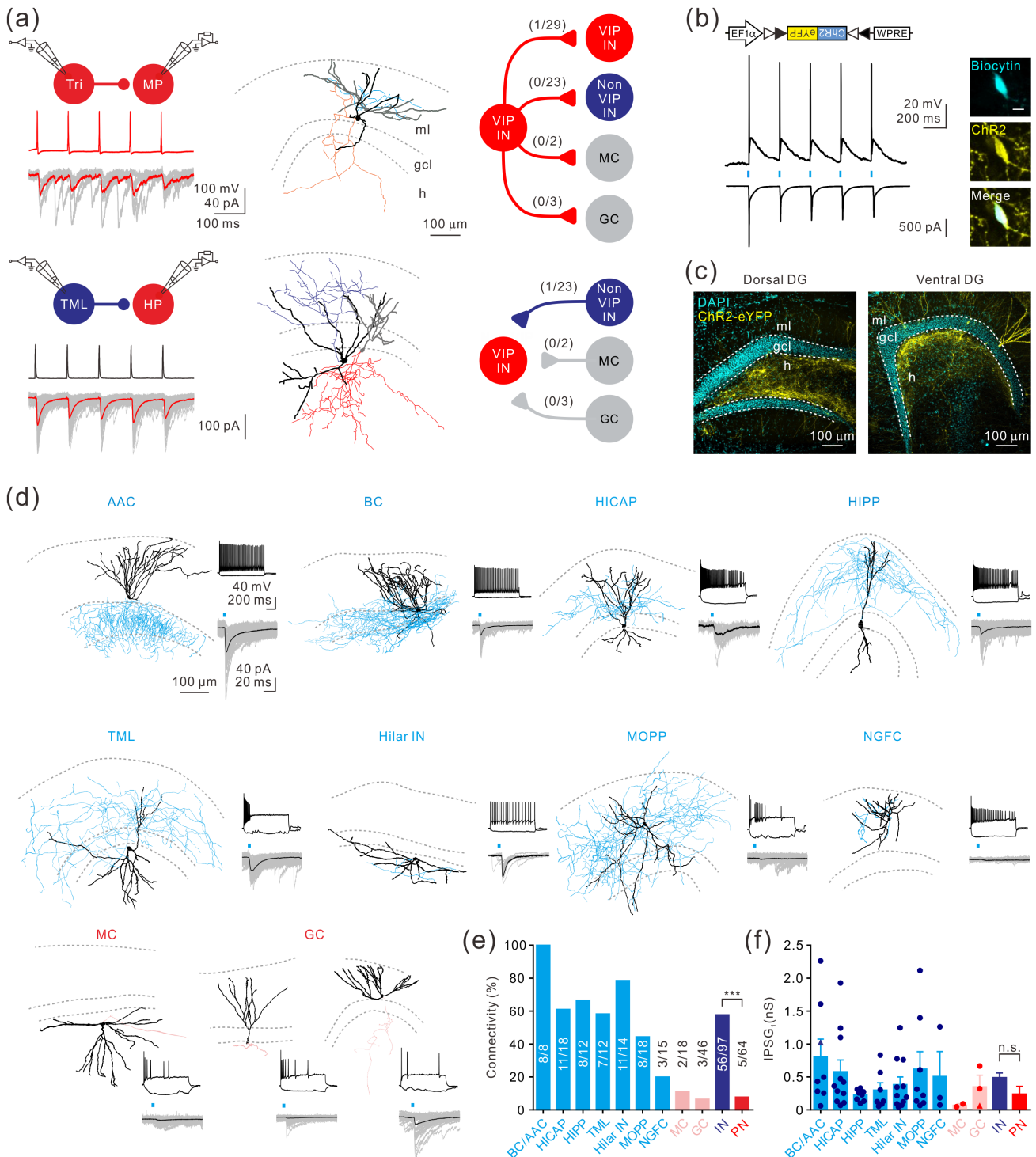


FIGURE 6 Legend on next page.

**TABLE 7** Properties of light-evoked IPSCs in DG neurons

	Synaptic delay <sup>a</sup> (ms)	20–80% rise time <sup>b</sup> (ms)	Decay $\tau$ (ms)	IPSG <sub>1</sub> (nS)	IPSG <sub>1/5</sub>
AAC (1)	2.3	.9	17.3	1.0	1.3
BC (7)	3.4 ± .9	1.7 ± .4	20.2 ± 7.2	.8 ± .3	1.3 ± .2
HICAP (11)	4.4 ± .6	2.2 ± .4	21.3 ± 2.7	.6 ± .2	1.4 ± .2
HIPP (8)	3.3 ± .5	2.7 ± .6	25.3 ± 8.5	.2	1.7 ± .2
TML (7)	2.9 ± .2	1.6 ± .2	18.4 ± 3.3	.3 ± .1	2.0 ± .6
Hilar IN (11)	3.9 ± .4	2.8 ± 1.0	26.7 ± 5.0	.4 ± .1	1.4 ± .3
MOPP (8)	6.7 ± 1.1	1.9 ± .3	17.0 ± 1.9	.6 ± .3	3.0 ± .7
NGFC (3)	5.1 ± 2.0	2.9 ± 1.7	21.7 ± 5.5	.5 ± .4	1.3 ± .2
MC (2)	2.0	4.5	21.7	.1	.8
GC (3)	5.8 ± .7	1.4 ± .4	21.1 ± 4.4	.3 ± .2	.6 ± .1

Note: The numbers of cells were provided in parentheses. All values were expressed as mean ± SEM.

Abbreviations: BC, basket cell; HICAP, hilar commissural-associational pathway-associated cell; HIPP, hilar perforant path-associated cell; MOPP, molecular layer perforant path-associated cell; NGFC, neurogliaform cell; TML, total molecular layer interneuron.

<sup>a</sup>Synaptic delay was calculated as the time elapsed from the onset of photo-stimulation to the onset of the first monosynaptic EPSC.

<sup>b</sup>20–80% rise time was measured from the first monosynaptic IPSC.

**FIGURE 7** Synaptic strength of PV<sup>+</sup> and SST<sup>+</sup> INs in the DG circuitry. (a) ChR2-eYFP expression patterns in the PV-Cre mice. Note the pronounced eYFP signal in the perisomatic areas. (b) IR-DGC and epifluorescent images. Note that a dense signal was observed in the gcl. (c) Top, schematic illustration. PV<sup>+</sup> cells were excited by 470 nm light, which was delivered through the objective lens. Bottom, representative IPSCs were recorded from a GC (left), and quantification of IPSG elicited by optogenetic stimulation of PV<sup>+</sup> cells (right). IPSG, 7.5 ± 1.8 nS, *n* = 8. (d–f) Same strategies were applied using SST-Cre mice. IPSG, 1.3 ± .2 nS, *n* = 12. Data were expressed as mean ± SEM. (g–h) Connectivity and IPSG of three distinct GABAergic synapses. Data were expressed as mean ± SEM [Color figure can be viewed at [wileyonlinelibrary.com](http://wileyonlinelibrary.com)]

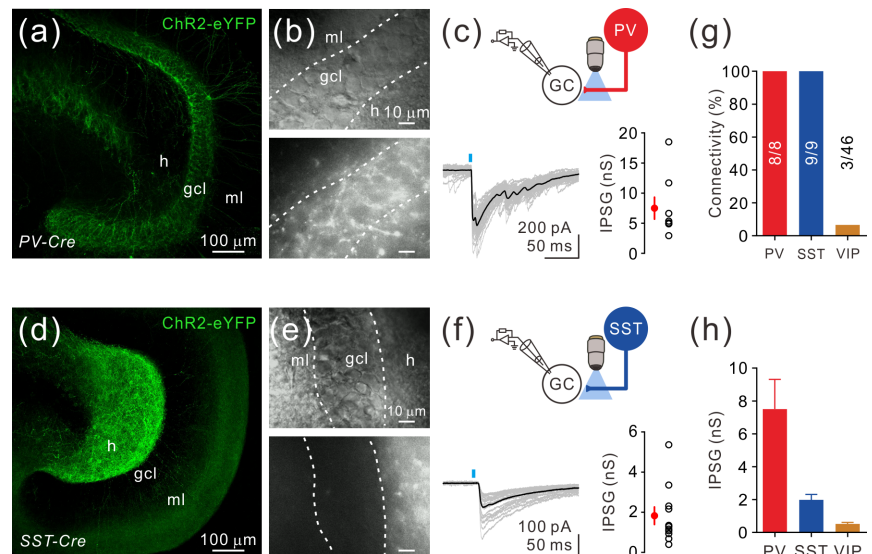


**FIGURE 6** VIP<sup>+</sup> INs preferentially innervate DG INs. (a) Left, evoked presynaptic action potentials, and unitary synaptic currents were recorded from INs simultaneously. Middle, reconstructions of a Tri – MP VIP<sup>+</sup> IN pair and TML-like IN- HP VIP<sup>+</sup> IN pair. Soma and dendrites of presynaptic and postsynaptic neurons were shown in black and gray, respectively. Axonal arborization of the presynaptic and postsynaptic VIP<sup>+</sup> INs were shown in the same color codes as in Figure 3(a). The axons of TML-like INs were in blue. The presynaptic IN was stimulated by current pulse injection at 10-Hz. Right, summary of all recorded pairs in the DG. (b) Schematic diagram of the viral DIO-ChR2 construct. 5-ms light pulses at 5-Hz evoked spikes recorded in an eYFP<sup>+</sup> IN in current clamp at –60 mV and ChR2-mediated photocurrents recorded in voltage clamp at –60 mV. Scale bar for the recorded cell = 10 μm. (c) ChR2-eYFP and DAPI expression patterns in the dorsal and ventral DG after 3 weeks of viral injection. Note the dense eYFP signal expressed in the hilus. (d) Exemplar reconstructions, firing patterns (–50 and 500 pA), and light-evoked IPSCs recorded in different types of DG cells. Somata and dendrites were shown in black. The axons of the inhibitory INs and excitatory PN were shown in blue and red, respectively. (e) Connectivity between VIP<sup>+</sup> INs and different types of DG cells. The averages of VIP<sup>+</sup> IN-IN and VIP<sup>+</sup> IN-PN connectivity were shown in dark bars (\*\*\*) *p* < .001; two-tailed Fisher's exact test). BC, basket cell; HICAP, hilar commissural-associational pathway-associated cell; HIPP, hilar perforant path-associated cell; TML, total molecular layer interneuron; MOPP, molecular layer perforant path-associated cell; NGFC, neurogliaform cell. (f) Summary of the first IPSG (IPSG<sub>1</sub>) recorded from different cell types. Only cells with functional connections with presynaptic VIP<sup>+</sup> cells were included here. Individual cells were shown in circles (one AAC and one GC were shown in triangle). The averages of IPSG<sub>1</sub> at VIP<sup>+</sup> IN-IN and VIP<sup>+</sup> IN-PN connections were shown in dark bars (n.s., no significant difference; Mann-Whitney U-test). Data were expressed as mean ± SEM [Color figure can be viewed at [wileyonlinelibrary.com](http://wileyonlinelibrary.com)]

Most DG INs are known to innervate GCs directly through the feedback and feedforward inhibition. However, little is known about the synaptic role of IN-selective INs in these microcircuits. To examine the cell-type specific projection from distinct classes of VIP<sup>+</sup> INs, we performed paired-recording. Unfortunately, VIP<sup>+</sup> INs form synapses with postsynaptic neurons with low connectivity. Alternatively, we used an optogenetic approach to address this issue. The result of optogenetic-assisted circuit mapping indicates that VIP<sup>+</sup> INs rarely target glutamatergic PNs (i.e., GCs and MCs), but are specialized in innervating other INs.

Different IN types are shown to control network activity during behavior (Lapray et al., 2012). In cortical regions, VIP<sup>+</sup> INs suppress the firing of other local INs during complex behaviors, including locomotion, visual processing, and other sensory reinforcement (Fu et al., 2014; Garcia-Junco-Clemente et al., 2017; Jackson, Ayzenshtat, Karnani, & Yuste, 2016; Mardinly et al., 2016; Pi et al., 2013). VIP<sup>+</sup> INs are active when the mouse is whisking, whereas they are inactive during non-whisking periods, thereby providing an activity-dependent gain control through disinhibition (Lee et al., 2013). The DG activity is critical to cognitive processes such as pattern separation and mood regulation (Anacker et al., 2018; Burghardt, Park, Hen, & Fenton, 2012; Engin et al., 2016). Our results indicate that VIP<sup>+</sup> INs in the DG are also primarily involved in disinhibitory modulation of the network. Their intrinsic properties and synaptic dynamics further suggest that they are recruited to ongoing activity with a certain latency. However, to better understand their network function, in vivo experiments with freely moving animals using behavioral paradigms will be required.

## ACKNOWLEDGMENTS

The authors thank Dr. D. Engel for commenting on an earlier version of the manuscript and all the members of the Lien lab for insightful discussions. This work was financially supported by the German Research Foundation (DFG project no. 384230557 to I.V.), Brain Research Center, National Yang-Ming University from the Featured Areas Research Center Program within the framework of the Higher Education Sprout Project by the Ministry of Education, National Health Research Institutes (NHRI-EX109-10814NI), and Ministry of Science and Technology (MOST 106-2320-B-010-011-MY3, MOST-DFG joint grant 106-2923-B-010-001-MY3, 108-2923-B-010-001-MY2, 108-2911-I-010-504, 108-2321-B-010-009-MY2, 108-2320-B-010-026-MY3, 108-2638-B-010-002-MY2) in Taiwan.

## AUTHOR CONTRIBUTIONS

Yu-Ting Wei, Imre Vida, and Cheng-Chang Lien designed the experiments and wrote the article. Yu-Ting Wei, Chia-Wei Yeh, and Hung-Chang Shen executed the experiments. Yu-Ting Wei, Jei-Wei Wu, Kun-Pin Wu, and Cheng-Chang Lien analyzed the data. Imre Vida and Cheng-Chang Lien performed funding acquisition.

## PEER REVIEW

The peer review history for this article is available at <https://publons.com/publon/10.1002/cne.25116>.

## DATA AVAILABILITY STATEMENT

The data that support the findings of this study are available from the corresponding author (C.C.L.) upon reasonable request.

## ORCID

Yu-Ting Wei  <https://orcid.org/0000-0003-3492-3113>

Imre Vida  <https://orcid.org/0000-0003-3214-2233>

Cheng-Chang Lien  <https://orcid.org/0000-0002-6692-9942>

## REFERENCES

- Acsády, L., Görcs, T. J., & Freund, T. F. (1996). Different populations of vasoactive intestinal polypeptide-immunoreactive interneurons are specialized to control pyramidal cells or interneurons in the hippocampus. *Neuroscience*, 73, 317–334. [https://doi.org/10.1016/0306-4522\(95\)00609-5](https://doi.org/10.1016/0306-4522(95)00609-5)
- Anacker, C., Luna, V. M., Stevens, G. S., Millette, A., Shores, R., Jimenez, J. C., Chen, B., & Hen, R. (2018). Hippocampal neurogenesis confers stress resilience by inhibiting the ventral dentate gyrus. *Nature*, 559, 98–102. <https://doi.org/10.1038/s41586-018-0262-4>
- Armstrong, C., Szabadics, J., Tamás, G., & Soltesz, I. (2011). Neurogliaform cells in the molecular layer of the dentate gyrus as feed-forward  $\gamma$ -aminobutyric acidergic modulators of entorhinal-hippocampal interplay. *Journal of Comparative Neurology*, 519, 1476–1491. <https://doi.org/10.1002/cne.22577>
- Burghardt, N. S., Park, E. H., Hen, R., & Fenton, A. A. (2012). Adult-born hippocampal neurons promote cognitive flexibility in mice. *Hippocampus*, 22, 1795–1808. <https://doi.org/10.1002/hipo.22013>
- Chiang, P. H., Wu, P. Y., Kuo, T. W., Liu, Y. C., Chan, C. F., Chien, T. C., Cheng, J. K., Huang, Y. Y., Chiu, C. D., & Lien, C. C. (2012). GABA is depolarizing in hippocampal dentate granule cells of the adolescent and adult rats. *Journal of Neuroscience*, 32, 62–67. <https://doi.org/10.1523/JNEUROSCI.3393-11.2012>
- Donato, F., Rompani, S. B., & Caroni, P. (2013). Parvalbumin-expressing basket-cell network plasticity induced by experience regulates adult learning. *Nature*, 504, 272–276. <https://doi.org/10.1038/nature12866>
- Engin, E., Smith, K. S., Gao, Y., Nagy, D., Foster, R. A., Tsvetkov, E., Keist, R., Crestani, F., Fritschy, J. M., Bolshakov, V. Y., Hajos, M., Heldt, S. A., & Rudolph, U. (2016). Modulation of anxiety and fear via distinct intrahippocampal circuits. *eLife*, 5, e14120. <https://doi.org/10.7554/eLife.14120.001>
- Ewell, L. A., & Jones, M. V. (2010). Frequency-tuned distribution of inhibition in the dentate gyrus. *Journal of Neuroscience*, 30, 12597–12607. <https://doi.org/10.1523/JNEUROSCI.1854-10.2010>
- Fanselow, M. S., & Dong, H. W. (2010). Are the dorsal and ventral hippocampus functionally distinct structures? *Neuron*, 65, 7–19. <https://doi.org/10.1016/j.neuron.2009.11.031>
- Fenno, L. E., Mattis, J., Ramakrishnan, C., Hyun, M., Lee, S. Y., He, M., Tucciarone, J., Selimbeyoglu, A., Berndt, A., Grosenick, L., Zalocusky, K. A., Bernstein, H., Swanson, H., Perry, C., Diester, I., Boyce, F. M., Bass, C. E., Neve, R., Huang, Z. J., & Deisseroth, K. (2014). Targeting cells with single vectors using multiple-feature Boolean logic. *Nature Methods*, 11, 763–772. <https://doi.org/10.1038/nmeth.2996>
- Francavilla, R., Villette, V., Luo, X., Chamberland, S., Muñoz-Pino, E., Camiré, O., Wagner, K., Kis, V., Somogyi, P., & Topolnik, L. (2018). Connectivity and network state-dependent recruitment of long-range VIP-GABAergic neurons in the mouse hippocampus. *Nature Communications*, 9, 5043. <https://doi.org/10.1038/s41467-018-07162-5>
- Freund, T. F., & Buzsáki, G. (1996). Interneurons of the hippocampus. *Hippocampus*, 6, 347–470. [https://doi.org/10.1002/\(SICI\)1098-1063\(1996\)6:4<347::AID-HIPO1>3.0.CO;2-I](https://doi.org/10.1002/(SICI)1098-1063(1996)6:4<347::AID-HIPO1>3.0.CO;2-I)
- Fu, Y., Tucciarone, J. M., Espinosa, J. S., Sheng, N., Darcy, D. P., Nicoll, R. A., Huang, Z. J., & Stryker, M. P. (2014). A cortical circuit for

- gain control by behavioral state. *Cell*, 156, 1139–1152. <https://doi.org/10.1016/j.cell.2014.01.050>
- Garcia-Junco-Clemente, P., Ikrar, T., Tring, E., Xu, X., Ringach, D. L., & Trachtenberg, J. T. (2017). An inhibitory pull-push circuit in frontal cortex. *Nature Neuroscience*, 20, 389–392. <https://doi.org/10.1038/nn.4483>
- Guerra, L., McGarry, L. M., Robles, V., Bielza, C., Larrañaga, P., & Yuste, R. (2011). Comparison between supervised and unsupervised classifications of neuronal cell types: A case study. *Developmental Neurobiology*, 71, 71–82. <https://doi.org/10.1002/dneu.20809>
- Gulyás, A. I., Hájos, N., & Freund, T. F. (1996). Interneurons containing calretinin are specialized to control other interneurons in the rat hippocampus. *Journal of Neuroscience*, 16, 3397–3411. <https://doi.org/10.1523/JNEUROSCI.16-10-03397.1996>
- Gupta, A., Elgammal, F. S., Proddutur, A., Shah, S., & Santhakuma, V. (2012). Decrease in tonic inhibition contributes to increase in dentate semilunar granule cell excitability after brain injury. *Journal of Neuroscience*, 32, 2523–2537. <https://doi.org/10.1523/jneurosci.4141-11.2012>
- Hainmueller, T., & Bartos, M. (2020). Dentate gyrus circuits for encoding, retrieval and discrimination of episodic memories. *Nature Reviews Neuroscience*, 21, 153–168. <https://doi.org/10.1038/s41583-019-0260-z>
- Hájos, N., Acsády, L., & Freund, T. F. (1996). Target selectivity and neurochemical characteristics of VIP-immunoreactive interneurons in the rat dentate gyrus. *European Journal of Neuroscience*, 8, 1415–1431. <https://doi.org/10.1111/j.1460-9568.1996.tb01604.x>
- Halasy, K., & Somogyi, P. (1993). Subdivisions in the multiple GABAergic innervation of granule cells in the dentate gyrus of the rat hippocampus. *European Journal of Neuroscience*, 5, 411–429. <https://doi.org/10.1111/j.1460-9568.1993.tb00508.x>
- Hefft, S., & Jonas, P. (2005). Asynchronous GABA release generates long lasting inhibition at a hippocampal interneuron-principal neuron synapse. *Nature Neuroscience*, 8, 1319–1328. <https://doi.org/10.1038/nn1542>
- Hosp, J. A., Strüber, M., Yanagawa, Y., Obata, K., Vida, I., Jonas, P., & Bartos, M. (2014). Morpho-physiological criteria divide dentate gyrus interneurons into classes. *Hippocampus*, 24, 189–203. <https://doi.org/10.1002/hipo.22214>
- Hou, W. H., Kuo, N., Fang, G. W., Huang, H. S., Wu, K. P., Zimmer, A., Cheng, J. K., & Lien, C. C. (2016). Wiring specificity and synaptic diversity in the mouse lateral central amygdala. *Journal of Neuroscience*, 36, 4549–4563. <https://doi.org/10.1523/JNEUROSCI.3309-15.2016>
- Hsu, T. T., Lee, C. T., Tai, M. H., & Lien, C. C. (2016). Differential recruitment of dentate gyrus interneuron types by commissural versus perforant pathways. *Cerebral Cortex*, 26, 2715–2727. <https://doi.org/10.1093/cercor/bhv127>
- Hu, H., Gan, J., & Jonas, P. (2014). Interneurons. Fast-spiking, parvalbumin<sup>+</sup> GABAergic interneurons: From cellular design to microcircuit function. *Science*, 345, 1255–1263. <https://doi.org/10.1126/science.1255263>
- Jackson, J., Ayzenshtat, I., Karnani, M. M., & Yuste, R. (2016). VIP<sup>+</sup> interneurons control neocortical activity across brain states. *Journal of Neurophysiology*, 115, 3008–3017. <https://doi.org/10.1152/jn.01124.2015>
- Kheirbek, M. A., Drew, L. J., Burghardt, N. S., Costantini, D. O., Tannenholz, L., Ahmari, S. E., Zeng, H., Fenton, A. A., & Hen, R. (2013). Differential control of learning and anxiety along the dorsoventral axis of the dentate gyrus. *Neuron*, 77, 955–968. <https://doi.org/10.1016/j.neuron.2012.12.038>
- Kress, G. J., Dowling, M. J., Meeks, J. P., & Mennerick, S. (2008). High threshold, proximal initiation, and slow conduction velocity of action potentials in dentate granule neuron mossy fibers. *Journal of Neurophysiology*, 100, 281–291. <https://doi.org/10.1152/jn.90295.2008>
- Krueppel, R., Remy, S., & Beck, H. (2011). Dendritic integration in hippocampal dentate granule cells. *Neuron*, 71, 512–528. <https://doi.org/10.1016/j.neuron.2011.05.043>
- Lapray, D., Laszotzci, B., Lagler, M., Viney, T. J., Katona, L., Valenti, O., Hartwich, K., Borhegyi, Z., Somogyi, P., & Klausberger, T. (2012). Behavior-dependent specialization of identified hippocampal interneurons. *Nature Neuroscience*, 15, 1265–1271. <https://doi.org/10.1038/nn.3176>
- Lee, C. T., Kao, M. H., Hou, W. H., Wei, Y. T., Chen, C. L., & Lien, C. C. (2016). Causal evidence for the role of specific GABAergic interneuron types in entorhinal recruitment of dentate granule cells. *Scientific Reports*, 6, 36885. <https://doi.org/10.1038/srep36885>
- Lee, S., Kruglikov, I., Huang, Z. J., Fishell, G., & Rudy, B. (2013). A disinhibitory circuit mediates motor integration in the somatosensory cortex. *Nature Neuroscience*, 16, 1662–1670. <https://doi.org/10.1038/nn.3544>
- Leutgeb, J. K., Leutgeb, S., Moser, M. B., & Moser, E. I. (2007). Pattern separation in the dentate gyrus and CA3 of the hippocampus. *Science*, 315, 961–966. <https://doi.org/10.1126/science.1135801>
- Lien, C. C., Martina, M., Schultz, J. H., Ehmke, H., & Jonas, P. (2002). Gating, modulation and subunit composition of voltage-gated K<sup>+</sup> channels in dendritic inhibitory interneurons of rat hippocampus. *Journal of Physiology*, 538, 405–419. <https://doi.org/10.1113/jphysiol.2001.013066>
- Liu, Y., Fujise, N., & Kosaka, T. (1996). Distribution of calretinin immunoreactivity in the mouse dentate gyrus. I. General description. *Experimental Brain Research*, 108, 389–403. <https://doi.org/10.1007/BF00227262>
- Liu, Y. C., Cheng, J. K., & Lien, C. C. (2014). Rapid dynamic changes of dendritic inhibition in the dentate gyrus by presynaptic activity patterns. *Journal of Neuroscience*, 34, 1344–1357. <https://doi.org/10.1523/JNEUROSCI.2566-13.2014>
- Madisen, L., Zwingman, T. A., Sunkin, S. M., Oh, S. W., Zariwala, H. A., Gu, H., Ng, L. L., Palmiter, R. D., Hawrylycz, M. J., Jones, A. R., Lein, E. S., & Zeng, H. (2010). A robust and high-throughput Cre reporting and characterization system for the whole mouse brain. *Nature Neuroscience*, 13, 133–140. <https://doi.org/10.1038/nn.2467>
- Mardinly, A. R., Spiegel, I., Patrizi, A., Centofante, E., Bazinet, J. E., Tzeng, C. P., Mandel-Brehm, C., Harmin, D. A., Adesnik, H., Fagioli, M., & Greenberg, M. E. (2016). Sensory experience regulates cortical inhibition by inducing IGF1 in VIP neurons. *Nature*, 531, 371–375. <https://doi.org/10.1038/nature17187>
- Marlin, B. J., Mitre, M., D'Amour, J. A., Chao, M. V., & Froemke, R. C. (2015). Oxytocin enables maternal behaviour by balancing cortical inhibition. *Nature*, 520, 499–504. <https://doi.org/10.1038/nature14402>
- Martina, M., Schultz, J. H., Ehmke, H., Monyer, H., & Jonas, P. (1998). Functional and molecular differences between voltage-gated K<sup>+</sup> channels of fast-spiking interneurons and pyramidal neurons of rat hippocampus. *Journal of Neuroscience*, 18, 8111–8125. <https://doi.org/10.1523/JNEUROSCI.18-20-08111.1998>
- Milner, B., Corkin, S., & Teuber, H. L. (1968). Further analysis of the hippocampal amnesic syndrome: 14-year follow-up study of H.M. *Neuropsychologia*, 6, 215–234. [https://doi.org/10.1016/0028-3932\(68\)90021-3](https://doi.org/10.1016/0028-3932(68)90021-3)
- Miyoshi, G., Hjerling-Leffler, J., Karayannis, T., Sousa, V. H., Butt, S. J., Battiste, J., Johnson, J. E., Machold, R. P., & Fishell, G. (2010). Genetic fate mapping reveals that the caudal ganglionic eminence produces a large and diverse population of superficial cortical interneurons. *Journal of Neuroscience*, 30, 1582–1594. <https://doi.org/10.1523/JNEUROSCI.4515-09.2010>
- Pernía-Andrade, A. J., & Jonas, P. (2014). Theta-gamma-modulated synaptic currents in hippocampal granule cells in vivo define a mechanism for network oscillations. *Neuron*, 8, 140–152. <https://doi.org/10.1016/j.neuron.2013.09.046>
- Pfeffer, C. K., Xue, M., He, M., Huang, Z. J., & Scanziani, M. (2013). Inhibition of inhibition in visual cortex: The logic of connections between molecularly distinct interneurons. *Nature Neuroscience*, 16, 1068–1076. <https://doi.org/10.1038/nn.3446>

- Pi, H. J., Hangya, B., Kvitsiani, D., Sanders, J. I., Huang, Z. J., & Kepecs, A. (2013). Cortical interneurons that specialize in disinhibitory control. *Nature*, *503*, 521–524. <https://doi.org/10.1038/nature12676>
- Pouille, F., & Scanziani, M. (2004). Routing of spike series by dynamic circuits in the hippocampus. *Nature*, *429*, 717–723. <https://doi.org/10.1038/nature02615>
- Prönneke, A., Scheuer, B., Wagener, R. J., Möck, M., Witte, M., & Staiger, J. F. (2015). Characterizing VIP neurons in the barrel cortex of VIPcre/tdTomato mice reveals layer-specific differences. *Cerebral Cortex*, *25*, 4854–4868. <https://doi.org/10.1093/cercor/bhv202>
- Rousseeuw, P. J. (1987). Silhouettes: A graphical aid to the interpretation and validation of cluster analysis. *Journal of Computational and Applied Mathematics*, *20*, 53–65. [https://doi.org/10.1016/0377-0427\(87\)90125-7](https://doi.org/10.1016/0377-0427(87)90125-7)
- Rudy, B., Fishell, G., Lee, S., & Hjerling-Leffler, J. (2011). Three groups of interneurons account for nearly 100% of neocortical GABAergic neurons. *Developmental Neurobiology*, *71*, 45–61. <https://doi.org/10.1002/dneu.20853>
- Scharfman, H. E., & Myers, C. E. (2013). Hilar mossy cells of the dentate gyrus: A historical perspective. *Frontiers in Neural Circuits*, *6*, 106. <https://doi.org/10.3389/fncir.2012.00106>
- Scoville, W. B., & Milner, B. (1957). Loss of recent memory after bilateral hippocampal lesions. *Journal of Neurology, Neurosurgery, and Psychiatry*, *20*, 11–21. <https://doi.org/10.1136/jnnp.20.1.11>
- Taniguchi, H., He, M., Wu, P., Kim, S., Paik, R., Sugino, K., Kvitsiani, D., Fu, Y., Lu, J., Lin, Y., Miyoshi, G., Shima, Y., Fishell, G., Nelson, S. B., & Huang, Z. J. (2011). A resource of Cre driver lines for genetic targeting of GABAergic neurons in cerebral cortex. *Neuron*, *71*, 995–1013. <https://doi.org/10.1016/j.neuron.2011.07.026>
- Turi, G. F., Li, W. K., Chavlis, S., Pandi, I., O'Hare, J., Priestley, J. B., Grosmark, A. D., Liao, Z., Ladow, M., Zhang, J. F., Zemelman, B. V., Poirazi, P., & Losonczy, A. (2019). Vasoactive intestinal polypeptide-expressing interneurons in the hippocampus support goal-oriented spatial learning. *Neuron*, *101*, 1150–1165. <https://doi.org/10.1016/j.neuron.2019.01.009>
- Tyan, L., Chamberland, S., Magnin, E., Camiré, O., Francavilla, R., David, L. S., Deisseroth, K., & Topolnik, L. (2014). Dendritic inhibition provided by interneuron-specific cells controls the firing rate and timing of the hippocampal feedback inhibitory circuitry. *Journal of Neuroscience*, *34*, 4534–4547. <https://doi.org/10.1523/JNEUROSCI.3813-13.2014>
- Wakeham, C. M., Ren, G., & Morgans, C. W. (2020). Expression and distribution of trophoblast glycoprotein in the mouse retina. *Journal of Comparative Neurology*, *528*, 1660–1671. <https://doi.org/10.1002/cne.24850>
- Wall, N. R., De La Parra, M., Sorokin, J. M., Taniguchi, H., Huang, Z. J., & Callaway, E. M. (2016). Brain-wide maps of synaptic input to cortical interneurons. *Journal of Neuroscience*, *36*, 4000–4009. <https://doi.org/10.1523/JNEUROSCI.3967-15.2016>
- Ward, J. H. (1963). Hierarchical grouping to optimize an objective function. *Journal of the American Statistical Association*, *58*, 236–244. <https://doi.org/10.1080/01621459.1963.10500845>
- Yu, J., Swietek, B., Proddatur, A., & Santhakumar, V. (2015). Dentate total molecular layer interneurons mediate cannabinoid-sensitive inhibition. *Hippocampus*, *25*, 884–889. <https://doi.org/10.1002/hipo.22419>
- Yuan, M., Meyer, T., Benkowitz, C., Savanthrapadian, S., Ansel-Bollepalli, L., Foggetti, A., Wulff, P., Alcami, P., Elgueta, C., & Bartos, M. (2017). Somatostatin-positive interneurons in the dentate gyrus of mice provide local- and long-range septal synaptic inhibition. *eLife*, *6*, e211105. <https://doi.org/10.7554/eLife.211105>

**How to cite this article:** Wei Y-T, Wu J-W, Yeh C-W, et al. Morpho-physiological properties and connectivity of vasoactive intestinal polypeptide-expressing interneurons in the mouse hippocampal dentate gyrus. *J Comp Neurol*. 2021; 1–18. <https://doi.org/10.1002/cne.25116>